Treball de Fi de Grau

Grau en Enginyeria Física

Long-term morphodynamic evolution of the Llobregat Delta under climate change conditions

November 24, 2020

Author: Miquel Negre Dou

Directors: Francesca Ribas Prats and Albert Falqués Serra

Defense: 27/11/2020

e^{f}

Escola Tècnica Superior d'Enginyeria
de Telecomunicació de Barcelona

UPC

Abstract

Global warming will produce important effects at the coasts mainly due to sea level rise, which will increase the amount of inundation events and the erosion trends. The delta planes are particularly vulnerable because of their low altitudes, and this is especially critical if they are highly populated as occurs in the Llobregat delta (Barcelona). The present project focuses on the southern side of the delta, which consists of a long stretch of sandy coast ranging from the Garraf Mountain chain up to the groin of the Llobregat outfall. It includes the sandy beaches of the cities of Castelldefels, Gavà, Viladecans and El Prat. The management of such coastal erosion problems would strongly benefit from a good knowledge of the time dynamics of the system under different climate change scenarios.

The long-term evolution of sandy coasts is caused by gradients in the sediment transport, a very complex (and partially unknown) process driven by surface wave orbital motion and wave-driven mean currents. The corresponding sediment erosion and deposition patterns change the shoreline position and the sea bed, which in turn affects the wave and current dynamics. This can produce strong feedback processes and a rich nonlinear dynamical behaviour. The nonlinear Q2Dmorfo model (Arriaga *et al.*, 2017) is adequate to capture these mechanisms and hence to reproduce the evolution of the coast at scales from years to decades. It describes the propagation of monochromatic waves over the variable bathymetry using linear ray theory, computes the corresponding wave-driven alongshore sediment transport and includes the cross-shore transport in a simplified way. The essential simplification is that it does not resolve the full surf zone hydrodynamics. So far, the model has been mostly used assuming a constant sea surface level. However, the slow sea level rise due to global warming can influence the dynamics at such long-term time scales. Storm surges, that is, the mean sea level rise at the coast due to storms, can also play a role. Some improvements have been recently incorporated in the model (e.g., solid lateral boundary conditions, a variable sea level and alongshore-variable wave conditions). The Q2Dmorfo model, written in Fortran77 language, has been developed by the UPC research group where this TFG was done.

The model was first applied to the past observations at the southern side of the Llobregat delta data in order to validate it for a 5 year-long period (2012-2017). Finally, the model was forced with offshore data of the future 50 yr corresponding to different scenarios of climate change (including sea level rise). The wave conditions were based on measured past data. The available past data included hourly (alongshore-variable) wave conditions in front of the coast (at 10-20 m depth), hourly sea surface level at the Barcelona harbour, yearly shoreline positions extracted from aerial ortophotos, several topographies measured with LIDAR and a few bathymetries. The three latter data sets were provided by researchers form the Institut de Ciències del Mar (ICM, CSIC, Barcelona). The future sea level data was provided by researchers from the Institut Mediterrani d'Estudis Avançats (IMEDEA, Mallorca) and are based on the global projections made by Kopp *et al.* (2014).

Although most of the performed simulations blew up before reaching to predict for the desired lapse of time (due to an instability recently described in Falqués *et al.* (2020)), some general guidelines on the characteristic morphodynamic behaviour of the site have been established. All the sea level rise scenarios studied predict an overall regression of the domain shoreline, particularly accentuated in the region closest to the Llobregat mouth. For the most likely climate change scenario, a loss of 43 % of the initial dry beach area is predicted to occur by 2075.

e**f**

Contents

Acronyms

CERC Coastal Engineering Research Center.

ICM Institut de Ciències del Mar.

IMEDEA Institut Mediterrani d'Estudis Avançats.

LIDAR Laser Imaging, Detection and Raging.

MSL Mean Sea Level.

MSLR Mean Sea Level Rise.

NaN Not a Number.

NMMA Catalan or Spanish acronym for 'Mean sea level in Alacant'.

Q2Dmorfo Quasi-two-Dimensional morphodynamic model.

RCP Representative Concentration Pathway.

RMSE Root Mean Square Error.

RMSSS Root Mean Square Skill Score.

SLR Sea Level Rise.

SWAN Simulating WAves Nearshore.

UTM Universal Transverse Mercator.

ZM Zandmotor (Sand engine), mega-nourishment located on the Dutch Delfland coast.

e^f

1 Introduction

1.1 Motivation

Climate change has become one of the most important challenges that mankind will have to face during the following years. Its effects, some of them already visible nowadays, are expected to have a huge impact on the evolution of the coasts worldwide, and the Catalan coast is not an exception.

Being able to model and predict, within a certain degree of certainty, how a shoreline will evolve under different climate change scenarios can help us to prepare an appropriate response that guarantees the preservation of a beach. The aim of this project is to provide such type of predictions for the coastline of the Llobregat delta using the large-scale (both temporal and spatial) model *Q2Dmorfo*, which has been already successfully validated the Zandmotor site in the Netherlands (Arriaga, 2017).

Adapting and applying this model to the Llobregat delta will help to understand the dominant sediment transport processes driven by the wave climate and the corresponding morphodynamical trends. Moreover, applying the model in this particular case may also be useful for future studies in a similar context or setting. However, this project is not only interesting from an academic perspective but also from a practical point of view, since the Llobregat delta, besides playing a key role in the local economic and tourist scene, is also home of some of Catalonia's most relevant infrastructures, including the Josep Tarradellas international airport. Recent events, particularly the devastating storm Gloria in this early 2020, have evinced the necessity of devising a long-term plan in order to ensure the future of our coastline.

1.2 Coastal processes: morphodynamic changes and sediment transport

1.2.1 Dominant physical processes

The term morphodynamics, introduced into coastal literature by Wright and Thom in 1977, can be defined as *"the mutual adjustment of topography and fluid dynamics involving sediment transport"* (Short, 2000). Therefore, the study of the morphodynamics of a beach does not only imply investigating the topography of the site but also understanding how it behaves in relation to the sea, since a feedback relation exists between the evolving topography and the fluid motions produced by waves, tides or currents. The sediment transport produced by the hydrodynamics modifies the sea bed, which in turn will influence future sea motion and so on. This coupled and indivisible interaction adds more complexity to the already challenging fields of fluid dynamics and sediment transport; where turbulence, non-linearities, chaotic behaviour and theoretical uncertainties are common difficulties. The aforementioned factors, together with a time dependent stochastic forcing dependant of meteorology, and the interference of processes at different temporal and spatial scales, make addressing problems related to coastal morphodynamics extremely complicated, either using an experimental or modelling approach. In order to comprehend how the morphodynamic evolution of a beach can be modelled, first it is necessary to understand the basic physical processes.

Sediment transport usually refers to the combined movement of sediment as bedload (formed from particles which are at least partially in contact with the sea bed during the transport processes) and in suspension (formed from finer particles that are not normally represented in the bed). Waves and currents are the main cause of sediment transportation. Not all the bathymetry

e^f

is equally affected by sea motion, but there exist zones beyond a certain depth, called the depth of closure or D_c, the total sediment transport becomes negligible. That is, seaward of this depth although the waves can move sediment, the net sediment transport does not result in significant changes in mean water depth. The depth of closure is generally placed at the end of the zone known as the nearshore (see figure 1.2.1); its position depends on how exposed the beach is and the mean height of the wave climate. The more protected a beach and lower the waves, the narrower and shallower the nearshore zone. Moreover, the sediment transport is largest at the surf zone, the area where waves break and dissipate all its energy (extending all the way from the breaking depth, D_b, until the shoreline).

Littoral sediment transport is often decomposed in two categories depending on its direction with respect to the shoreline: alongshore and cross-shore. Nevertheless, this division should be purely seen as an artificial classification, useful to decouple and simplify processes when modelling, rather than a natural one. Alongshore transport describes the sediment motion along (parallel to) a coastline under the action of the waves and the ulterior longshore currents. These longshore currents are continuous shore-parallel flows within the surf zone that appear as a result of the energy dissipated by wave-breaking. One of the oldest and still most successful ways for predicting alongshore transport, the CERC (Coastal Engineering Research Center) formula (reviewed during section 3.2), grounds its basis on the assumption that the main driver of sediment in this direction are not tides nor ocean currents (not to be confused with nearshore/surf zone currents) but waves with an oblique incidence with respect to the shoreline that create the aforementioned longshore currents. Typically, the longshore sediment transport at a certain site will consist of a positive drift during part of the time and a negative one during the remainder. This kind of transport can be easily recognised in the accretion/erosion formed around breakwaters or other man-made infrastructures that interfere with the path of the longshore current. Cross-shore transport describes the sediment motion perpendicularly to the coastline, either on the seaward or landward direction. Whilst alongshore sediment transport is mostly due to the wave-induced longshore current, cross-shore transport is a consequence of the water motions that arise from incoming waves and the undertow current. The latter is an offshore directed current that flows underneath waves, near the sea bottom, as waves reach the shore. Its cause is the unbalance between radiation stresses (excess momentum fluxes) and pressure forces at different vertical locations. Despite having identified its main sources, and also in contrast with the alongshore case, the coupling between the hydrodynamics and the cross-shore transport is not well understood (Amoudry and Sousa, 2011). These unknowings and uncertainties, force some models to rely on simplifications and heuristic parameterisations to quantify the cross-shore transport (vital in shaping the beach profile).

Finally, it is important to remark that this project will be solely focused on the natural progression of the Llobregat delta and therefore no human interference, such as sand accumulation in man-made breakwaters or periodic beach nourishment, will be taken into account. Moreover, just the main natural mode of sediment transport will be addressed: waves and the subsequent currents that they generate. This implies that mechanisms like direct wind transport (mainly present in the sub-aerial beach) or the sediment contribution derived from fluvial or pluvial processes (rivers, creeks, ponds, channels, etc.) will be neglected. These decisions will be further discussed and properly justified for the chosen site in forthcoming sections 2.1 and 3.2.

1.2.2 Coastal morphodynamic models

Coastal morphodynamic evolution can be studied at many temporal and spatial scales, since the characteristic times and lengths of the different processes range from a few hours to decades and from tens of meters to several kilometers. Choosing one or another depends on the information (and accuracy) one is willing to obtain about a certain beach system. Modelling the effect of a storm on the surf zone, for instance, does require a small domain and a fine spatio-temporal mesh due to the high variability of the dominant phenomena studied. On the other extreme, shoreline recession due to sea level rise can take decades to even manifest. Expecting to simulate precisely all the scales with the same model is not only unrealistic but computationally unviable.

Another key parameter to be taken into account when modelling is the number of dimensions considered. One-line models (Kamphuis, 2000) only consider the alongshore sediment transport and assume instantaneous changes of the beach profile as cross-shore transport, which forbids them to accurately reproduce sediment transport during long periods of time (years-decades). On the other hand, one can find the two-dimensional models where the hydrodynamics in the surf-zone are also computed in order to obtain a more accurate estimate of the sediment transport and bed evolution. The precision of these models however, comes at the expense of computational agility, which makes them inappropriate for long-term runs (years-decades).

In a middle ground, the Q2Dmorfo (Quasi-two-Dimensional morphodynamic model) can be found (Falqués *et al.* 2008)). The Q2Dmorfo is a non-linear model for large-scale (1-100 km) shoreline-dynamics on medium to long-term scales (years-decades), based on the assumptions that shoreline dynamics is controlled by the gradients in the alongshore transport and that the cross-shore beach profiles tend to a previously defined equilibrium profile. Alongshore transport is parametrised directly from wave transformation, in a similar manner to the afore-mentioned one-line models (using the CERC formula). This transport does alter the initial beach profile, which is then assumed to tend to the stated equilibrium by means of a diffusive cross-shore transport. This transport is assumed to be stronger near the shoreline and to decay progressively, until reaching a residual value beyond the depth of closure. Due to the simplifications in the cross-shore transport and wave transformation, Q2Dmorfo can not model surf-zone morphodynamic patterns. However, these simplifications also allow Q2Dmorfo to tackle long-term simulations, as the ones intended in this project, in computationally reasonable times whilst maintaining an adequate certainty (Arriaga, 2017).
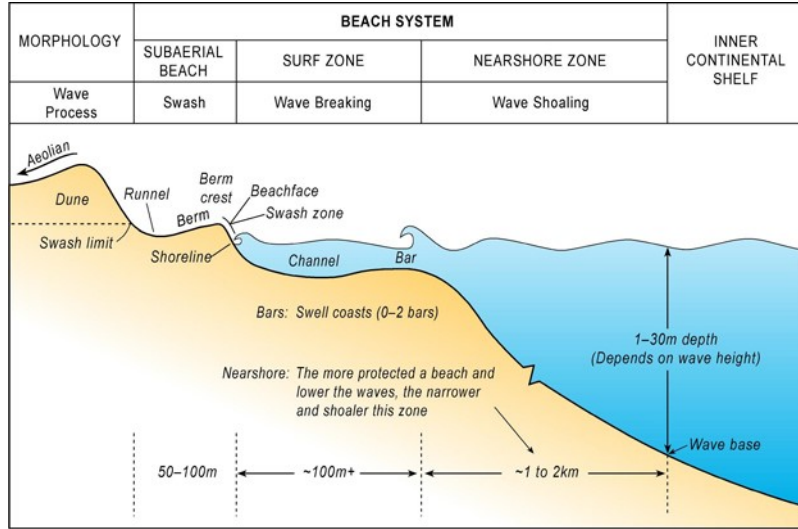
Figure 1.2.1: Definition sketch clarifying multiple coastal terms related to both sediment transport and wave propagation. Extracted from Arriaga (2017).

1.3   Coastal processes: wave propagation

Waves acquire energy from the wind blowing over the sea vastness. Meteorological phenomena as storms can endow tremendous amounts of energy to waves, which then can travel for thousands of kilometres towards the coastline almost unaltered. This energy accumulated over a large area of sea is then rapidly dissipated in a relatively narrow strip of the nearshore, on what it is commonly known as the surf zone(see figure 1.2.1).

In order to explain wave propagation towards the coast, first it is important to introduce some basic notions on linear or *Airy* theory for oceanic waters (those deep enough so that waves travelling there are not affected by the interaction with the seabed). Despite considering idealised physical conditions/motions for sea water (such as constant density or no viscosity) and assuming gravitation as the only external force, linear theory remains still as one of the robustest approaches to small-amplitude oceanic waves.

Airy theory is based on only two equations: mass or continuity balance and momentum conservation. In their linearised form, and having applied the assumptions of incompressible and inviscid fluids, they can be expressed as:

$$\nabla \cdot \vec{u} = \frac{\partial u_x}{\partial x} + \frac{\partial u_y}{\partial y} + \frac{\partial u_z}{\partial z} = 0 \quad , \quad \frac{\partial \vec{u}}{\partial t} = -\frac{1}{\rho}\nabla p - g\hat{z} \tag{1.1}$$

where $\vec{u}$ represents the velocity of the water particles in any of the three directions x, y or z, assigning the latter to the vertical coordinate (being $z = 0$ the still water level and $z = -d$ the seabed, assumed to be at a constant depth). Also during this section x will be regarded as the wave propagation direction, unless the contrary is stated. Furthermore, ρ and p are the water density and pressure, respectively. Finally, the letter g stands, of course, for Earth's gravity. Since potential flow is assumed, these equations can be rewritten in terms of the velocity potential, $\phi(x, y, z, t)$, that is defined such that $\vec{u} = \vec{\nabla}\phi$. Substituting in equation (1.1) one can find:

$$\Delta \phi = 0 \quad , \quad \frac{\partial \phi}{\partial t} + \frac{p}{\rho} + gz = f(t) \tag{1.2}$$

e**f**

the latter being the linearised Bernoulli equation for unsteady flow. In order to find reasonable solutions to these equations, specific boundary conditions or restrictions must be applied to each of the considered dimensions. The y dimension will be left unbounded assuming that the solution wave is periodic with infinitely long crests in this direction, which does make sense as length scales on oceanic and beach systems generally satisfy that $O(y) > O(x) >> O(z)$. Boundary conditions on the x coordinate will be considered fulfilled under the assumption that the solution to the equations will be periodic on this direction. Therefore, only boundary conditions along z-direction will be reviewed.

Since conservation of mass must be verified, water particles can not leave the sea surface. This is equivalent to saying that the normal velocity of a particle with respect to the surface must be equal to the speed of the surface in that direction. In its linearised version around $z = 0$ this can be expressed as $(u_z = \frac{\partial \phi}{\partial z} = \frac{\partial \eta}{\partial t})|_{z=0}$, where η is the surface elevation. A similar thing happens at sea bottom, since water particles shall not penetrate the seabed, their normal velocity there must be null: $(u_z = \frac{\partial \phi}{\partial z} = 0)|_{z=-d}$. Finally, in order to ensure that the wave is only subject to the action of gravity, pressure at sea surface should be constant (atmospheric), with the purpose of simplifying things $(p = 0)|_{z=0}$ will be taken. This last condition can be expressed as a function of the velocity potential: $(\frac{\partial \phi}{\partial t} + g\eta = 0)|_{z=0}$ using Bernoulli equation (1.2).

One of the solutions to the Laplace equation (1.2a) that satisfy the first two boundary conditions is a long-crested harmonic wave propagating in the positive x-direction: $\eta(x, t) = a \sin(\omega t - kx)$, where a, k and ω are the amplitude, the wavenumber and the angular frequency, respectively. From there, the velocity potential can be derived:

$$\phi = \frac{\omega a}{k} \frac{\cosh(k(d+z))}{\sinh(kd)} \cos(\omega t - kx) \tag{1.3}$$

Then, finding the velocities in each direction is immediate:

$$u_x = \omega a \frac{\cosh(k(d+z))}{\sinh(kd)} \sin(\omega t - kx), \quad u_y = 0, \quad u_z = \omega a \frac{\sinh(k(d+z))}{\sinh(kd)} \cos(\omega t - kx) \tag{1.4}$$

As expected the component y of the velocity is zero and all movement is concentrated in the x-z plane. With the aim of understanding better the motions of the water particles these expressions can be simplified making use of the fact that for large depths ($kd >> 1$) the velocities tend to $u_x = \omega a \exp(kz) \sin(\omega t - kx)$ and $u_z = \omega a \exp(kz) \cos(\omega t - kx)$, leaving a constant velocity module ($|\vec{u}|$) equal to $\omega a \exp(kz)$. If the previous simplified expressions are integrated, one can obtain the pathline for a water particle and, after a proper algebraic arrangement, a expression like the following can be found:

$$\frac{x^2}{a^2 e^{2kz}} + \frac{z^2}{a^2 e^{2kz}} = 1$$

As the reader may have already noticed, this formulation describes a circular movement of radii ae^{kz}. For shallower waters the premises under which these expressions were reached are no longer fulfilled and the motions become elliptical, causing an effect on seabed that may induce sediment stirring.

A dispersion relation can also be obtained replacing the expressions attained for η and ϕ into the last boundary condition, yielding: $\omega^2 = gk \tanh(kd)$. The phase velocity for harmonic waves can be computed as the ratio between the wavelength (λ) and the wave period (T), therefore:

$$c = \frac{\lambda}{T} = \frac{\omega}{k} = \sqrt{\frac{g}{k} \tanh(kd)}. \tag{1.5}$$

e^f

The group velocity is the propagation speed of the envelope of a group of waves of slightly different frequencies ans is also obtained from the dispersion relation as:

$$c_g = \frac{\partial \omega}{\partial k} = \frac{1}{2} \left(1 + \frac{2kd}{\sinh{(2kd)}} \right) c. \tag{1.6}$$

Finally, the wave energy per area of horizontal surface ($\Delta x \Delta y$)can be calculated by adding its potential and kinetic components. Wave induced potential energy ($\rho g z \Delta x \Delta y \Delta z$) in the entire column is equal to the potential energy difference between the presence and the absence of the wave. As we are interested in the potential energy per unit of area and time-averaged in one period, we get:

$$E_p = \overline{\int_{-d}^{\eta} \rho g z \, dz} - \overline{\int_{-d}^{0} \rho g z \, dz} = \overline{\int_{0}^{\eta} \rho g z \, dz} = \frac{1}{2} \rho g \overline{\eta^2} = \frac{1}{2} \rho g \left(\frac{a}{\sqrt{2}} \right)^2 = \frac{1}{4} \rho g a^2$$

For the kinetic energy ($\frac{1}{2} \rho \Delta x \Delta y \Delta z |\vec{u}|^2$) of the same time-averaged slice of water, one obtains:

$$E_k = \overline{\int_{-d}^{\eta} \frac{1}{2} \rho |\vec{u}|^2 \, dz} = \overline{\int_{-d}^{0} \frac{1}{2} \rho |\vec{u}|^2 \, dz} + \overline{\int_{0}^{\eta} \frac{1}{2} \rho \omega^2 a^2 e^{2kz} \, dz} \approx \overline{\int_{-d}^{0} \frac{1}{2} \rho |\vec{u}|^2 \, dz}$$

The previous approximation is justified on the basis that linear theory has an small-amplitude approach. Whilst the first integral has $O(a^2)$ (due to the term $|\vec{u}|^2 \propto a^2$), the latter has $O(a^3)$ due to the superior integral limit $\eta \propto a$, and as a result can be neglected. Ultimately, using the expression found earlier for $|\vec{u}|$ and the dispersion relation (taking into account that $d >> 1$), E_k and the total energy E can be found:

$$E_k \approx \overline{\int_{-d}^{0} \frac{1}{2} \rho \omega^2 a^2 e^{2kz} \, dz} = \frac{1}{4} \rho a^2 \frac{gk \tanh{(kd)}}{k(1 - e^{-2kd})^{-1}} \approx \frac{1}{4} \rho g a^2 \rightarrow E = E_k + E_p \approx \frac{1}{2} \rho g a^2 \tag{1.7}$$

It can also be proved that the wave energy flux or transport per unit of crest length is equal to $E\vec{c_g}$ (demonstration included in Holthuijsen (2007)). Even though these equations are not directly applicable for coastal waters, they will be helpful when explaining the processes that a wave undergoes during its propagation towards the shore.

1.3.1   Shoaling

As waves approximate the coast, the water where they travel becomes shallower and therefore, the effect of the seabed on their motion becomes less and less negligible. The theoretical limit where the wave-seabed interaction begins to be considerable enough and must be taken into account is known as the wave base. Some literature define the wave base as the beginning of the nearshore zone, and its depth is usually agreed to be $\sim \lambda/2$.

The process of shoaling, occurs when due to the effect of shallow waters, the wavelength and velocity phase of the harmonic wave decrease as depth does (equation 1.5), whilst maintaining its original frequency. These variations also influence the velocity group (equation 1.6), which provokes a change in the local wave energy and hence in its amplitude. The shallower the waters the wave crosses, the closer the group and phase velocity values get and the less dispersive the wave becomes (phase speed less dependent on frequency).

A way of understanding wave shoaling in more detail is by focusing on the energy conservation. Figure 1.3.1a illustrates this process, with a wave ray propagating with normal incidence

towards a straight coast through shallow waters, such that their bottom varies with a gentle slope. Now consider a volume G contained within the prism delimited by two vertical sides in the wave direction separated by a distance b, two vertical planes normal to the wave direction, the sea bottom and the sea surface. Since there is no flux of energy in any direction except for the one in which the wave propagates, and no dissipation or generation of waves takes place in volume G, the energy that enters through plane 1 (the one situated more seaward) must leave through plane 2. As Ec_g is the energy transport per unit of crest length, $Ec_g \cdot b$ must be the energy rate per unit time that crosses a plane of width b normal to the wave direction. Given that rates through planes 1 and 2 must be equal, and making use of expression (1.7), the following equivalence can be deduced :

$$E_1 c_{g,1} b = E_2 c_{g,2} b \rightarrow \frac{1}{2}\rho g a_1^2 c_{g,1} = \frac{1}{2}\rho g a_2^2 c_{g,2} \rightarrow a_2 = \sqrt{\frac{c_{g,1}}{c_{g,2}}} a_1 = K_{sh} a_1 \qquad (1.8)$$

If further inspection of equation (1.6) was conducted, one would see that, after a brief increment, group velocity decreases as sea bottom depth does. Consequently, for waters shallow enough $K_{sh} > 1$, which will translate into a growth of wave amplitude as waves propagate into shallower waters.

Of course this example is an idealisation of the mechanism of shoaling, devised to isolate this phenomena from other changing processes during wave propagation. Furthermore, one has to keep in mind that linear theory breaks long before the wave reaches the shoreline, otherwise the shoaling factor (K_{sh}) would become infinite there. In reality the shoaling process comes accompanied by an increase of non-linearity and asymmetry that eventually leads to wave-breaking, which cannot be characterised by *Airy* theory.
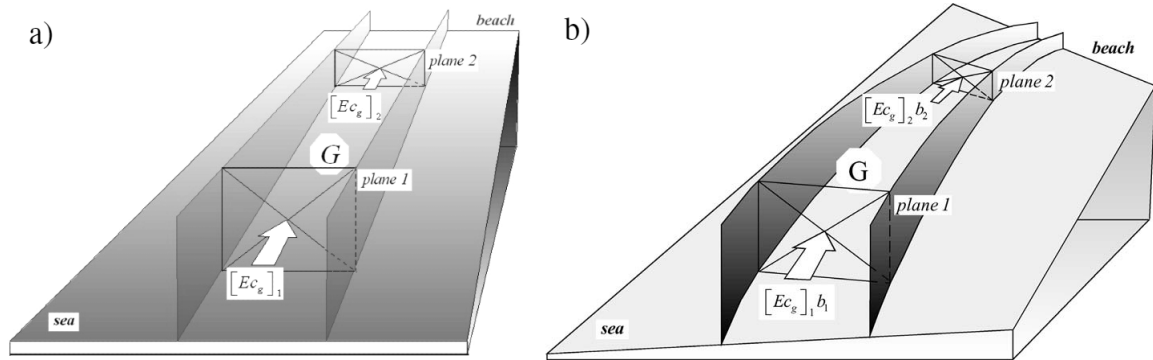

Figure 1.3.1: Energy conservation scenario examples for (a) purely wave shoaling and (b) wave refraction (b). Extracted from Holthuijsen (2007).

1.3.2 Refraction

When a wave advances towards the shoreline with a certain angle, or oblique incidence, it will slowly change its course as it approaches the coast. This deviation is caused by the velocity phase variation along the wave crest. Since parallel wave rays do not reach the same depth all at once, those at shallower waters travel slower than the ones at deeper waters (equation 1.5). Therefore, in a given time interval, the part of the crest above more profound waters will travel a larger distance than the part of the crest situated closer to the shore, resulting in a rotation of the wave front. *"This is a universal characteristic of waves: a wave always turns towards the region with lower propagation speed"* (Holthuijsen, 2007). In the case treated here, this region is the one with shallower waters.
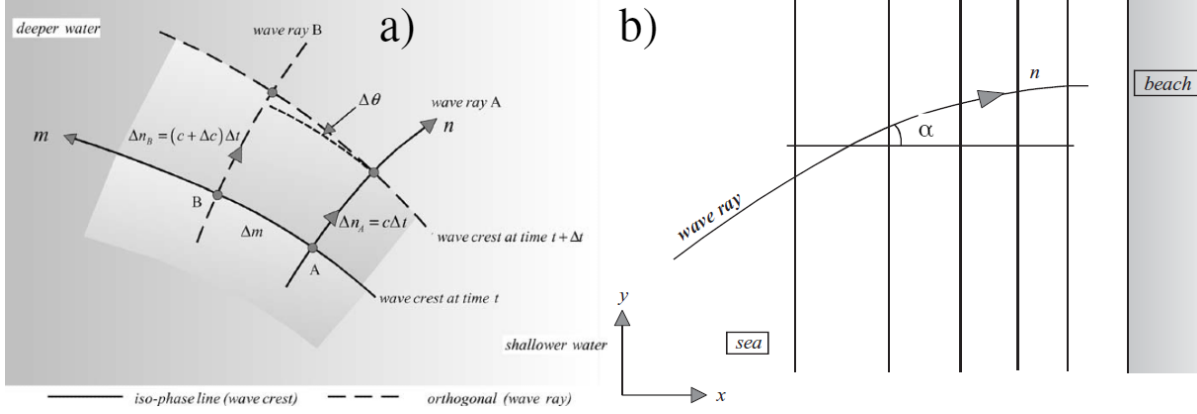
Figure 1.3.2: (a) General approach of wave turning rate computation. (b) Snell's law application, under the assumption of parallel depth contours. Extracted from Holthuijsen (2007).

To compute the turning rate of the wave consider two separated points, A and B, located along the wave crest direction $\hat{m}$ and that move normal to the crest, i.e. parallel to the wave propagation direction $\hat{n}$ (see figure 1.3.2a). Their position variation along axis $\hat{n}$ is: $\Delta n_A = c\Delta t$ and $\Delta n_B = (c+\Delta c)\Delta t$, respectively. Consider that Δc is positive with increasing m (implying that $\hat{m}$ points towards deeper waters) and that the crest turns clockwise, which in our reference system will be taken as negative ($\Delta\theta < 0$). Then: $\tan(\Delta\theta) \simeq \Delta\theta = -(\Delta n_B - \Delta n_A)/\Delta m = -\Delta c\Delta t/\Delta m$. However, we are interested in the infinitesimal spatial rate of turning ($\Delta\theta$) per unit of forward distance (Δn), that is to say, the curvature of the wave ray:

$$\frac{\Delta\alpha}{\Delta n} = -\frac{\Delta c\Delta t}{\Delta m\Delta n} = -\frac{\Delta c\Delta t)}{\Delta m(c\Delta t)} \xrightarrow{\Delta\to 0} \left(\frac{d\alpha}{dn}\right)_{ref} = -\frac{1}{c}\frac{\partial c}{\partial m} \tag{1.9}$$

In case of parallel depth contours, a much simpler approach is possible since Snell's law of refraction (figure 1.3.2b) can be directly applied:

$$\frac{d}{dn}\left(\frac{\sin\alpha}{c}\right) = 0 \to \frac{\sin\alpha}{c} = \text{constant} \to \sin\alpha = \frac{c}{c_{dw}}\sin\alpha_{dw} \tag{1.10}$$

where α is the angle between the wave propagation direction and the normal to the depth contours, whilst the sub-index dw indicates the wave properties at deep waters. From expression (1.10) one can conclude that for $c = 0$ wave direction will be $\alpha = 0$. This is the case when waves reach the shore, explaining why most waves arrive to the coast with perpendicular incidence independently of their original course in oceanic waters. Nonetheless, this is a theoretical result where effects like diffraction, complex topographies or wave-breaking are not taken into consideration.

Refraction does also have an effect on wave amplitude. In order to describe and estimate this change, a reasoning similar to the one used to yield equation (1.8) is taken. Nevertheless, now we treat with a wave with oblique incidence, and due to the effect of refraction, sides of volume G will be curvilinear (as illustrated in figure 1.3.1b), and planes 1 and 2 will not necessarily have the same width (b_1 and b_2 will represent the distance between two rays in oceanic and coastal waters, respectively). Following the same reasoning as that on the previous section, where no flux of energy does traverse volume G except for the one parallel to the wave propagation

direction, the next equivalence unfolds:

$$E_1 c_{g,1} b_1 = E_2 c_{g,2} b_2 \rightarrow \frac{b_1}{2}\rho g a_1^2 c_{g,1} = \frac{b_2}{2}\rho g a_2^2 c_{g,2} \rightarrow a_2 = \sqrt{\frac{c_{g,1}}{c_{g,2}}}\sqrt{\frac{b_1}{b_2}}a_1 = K_{sh}K_{ref}a_1 \quad (1.11)$$

A stretching of the wave crest as a result of refraction occurs for highly oblique waves and this provokes a dispersion of energy which is then reflected into a decrease of the wave amplitude.

1.3.3 Breaking

One of the most nonlinear and poorly understood phenomena in coastal waters is depth-induced wave breaking, when most of the energy carried by oceanic waves is dissipated. This energy release, by far the most important in the coastal zone, plays a key role in the formation of nearshore currents and consequently, on the transport of sediments that mold the morphology of a beach.

A wave breaks when it becomes overly steep (as the depth becomes shallower), *especially near the peak of its crest, because the velocities of water particles in the wave crest exceed the velocity of the wave form so that the crest surges ahead* (Komar, 1998). This wave asymmetry that provokes wave breaking comes as a result of the non-linearity introduced during the shoaling process. As seen in previous sections, when a wave advances into shallower waters its amplitude increases. However, this process cannot continue indefinitely and, eventually the wave becomes highly asymmetric and breaks.

Given the difficulty to locate where waves break, experts usually introduce an empiric parameter γ_b, which is commonly referred as the saturation ratio. Despite all the uncertainties inherent to the process of wave breaking, it is generally agreed that it occurs when wave height H_b is between 0.4 and 0.8 times the local water depth D_b:

$$H_b = \gamma_b D_b \quad \text{with} \quad \gamma_b \in [0.4, 0.8] \quad (1.12)$$

Once the wave breaks, disappearing into bubbles and foam, its energy transforms into heat and turbulence and induce sediment re-suspension and currents. The surf zone is the area with the most intense sediment transport precisely because of the high intensity of the turbulence provoked by wave breaking, which makes stirring sediment from the seabed easy.

1.4 Coastal processes: sea level variations

The water level of sea is ever changing with variations that can range from a few centimeters to several meters. This section will be devoted to describe and review in a qualitative manner the principal causes of sea level variation.

1.4.1 Astronomical tide

The daily rise and fall of tides is caused by the force exerted by the Sun and the Moon, combined with the effect of Earth's rotation, over vast bodies of water. The principal accountable to tides is the gravitational pull of the Moon. Nonetheless, this force is not homogeneous all around Earth's surface, and nowhere will the local force of attraction to water particles (f_a) be equal in magnitude and direction to the total force of attraction between the Earth and the Moon (F) (figure 1.4.1a). The difference between these forces at any point (figure 1.4.1b), results in a net force that has a component tangent to Earth's surface, and is mainly responsible of drawing water into tide bulges at both earthly extremes of the Earth-Moon axis (as depicted in figure 1.4.1c).
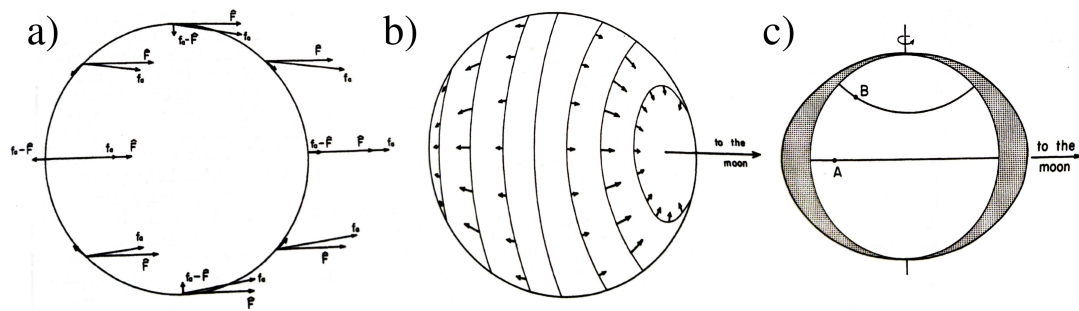
e**f**

Figure 1.4.1: (a) Moon gravitational pull distribution over Earth's surface, (b) the resulting tangential net force and (c) the idealistic bulges it creates in grey (c). Extracted from Komar (1998).

The Sun, despite its immense mass, creates a tide less than half of that of the Moon owing to its much larger distance from the Earth. However, its attraction does add or subtract to the sea level variation caused by the Moon. For instance, when the Earth, the Sun and the Moon are approximately aligned, solar and lunar tides add in the so-called spring-tides, whilst, when the Sun and the Moon are in quadrature (meaning that the gravitational pull of both celestial bodies operate at right angles to one another) the minimum tidal range is produced, also known as neap tides. Nevertheless, tides are not only dependent of gravitational forces, but effects derived from Earth's rotation such as Coriolis, or Earth's tilted axis with respect to the Equatorial plane, also play an important role in tidal behaviour.

Landmass or continental position is also relevant, and waters that are more landlocked (as the Mediterranean) tend to have lower tides (variations of a few centimeters) as a result of the narrow outlet/inlet with open bodies of water. There are locations, however, where tide-related variations can exceed several meters and have a serious impact on processes occurring within the nearshore, since the positions of the wave action and the shoreline migrate continuously. Tidal changes not only can give rise to currents, but also may have an effect on beach morphology and on cross-shore sediment distribution.

1.4.2   Storm surge

Storms (and other related meteorological phenomena such as typhoons, monsoons or hurricanes) consist of strong wind fields driven by pressure gradients from a central low pressure in the atmosphere. A storm surge consists of multiple components that contribute to sea level variations: the barometric tide, the wind-stress tide, and the wave set-up/down.

As aforementioned, storms form in a low pressure context and barometric tides are the direct response of coastal waters to this pressure gradient. At the center of the storm, water is sucked upwards by the low pressure air (surrounded by high pressure air), causing a sea over-elevation in that area that can be roughly computed using simple hydrodynamics. However, the sea level variation produced through this mechanism, around a few tens of centimeters, just accounts for a part of the whole storm surge effect.

The wind-stress tide is provoked by the frictional drag effect of wind blowing up over sea. To achieve an equilibrium in the cross-shore direction, a pressure-driven force arises, created by a sea surface slope in the wind direction. The greater the wind-stress, the steeper the resulting water surface slope is. Wind driven currents occur in the alongshore wind direction, in which case the hydrodynamic force equilibrium of the water column comes from a sea bottom shear-

stress that acts, by definition, against the direction of water movement.

Wave set-up is a water over-elevation that takes place where depth-induced wave-breaking occurs, and comes as a result of the momentum transfer process of these breaking waves to the water column (i.e. through gradients of the radiation stresses). In the case of shore-perpendicular wave incidence, the onshore momentum flux must be balanced by an equal and opposite force for equilibrium. This manifests itself as a slope in the mean still water level. For instance, before the breaker zone, shoaling confers the wave an amplitude increment and thus, an additional wave-induced flux of horizontal momentum, which can then only be compensated through a decrease of mean sea level (wave set-down). In contrast, after a wave breaks, energy flux is no longer constant but gradually depleted due to energy dissipation, with the consequent radiation stress reduction. In order to regain force balance a progressive increment of water surface has to take place (wave set-up). These descriptions however, are only valid for beaches with a mild slope and no abrupt depth variations. Set-down magnitude are quite small when compared to the set-up variation the second being $\sim 25\%$ of the breaking depth, D_b. The reason behind this, is that the radiation stress increment during shoaling is much less than the radiation stress decrease provoked by wave-breaking, when most of wave energy is scattered. As a consequence, set-up comprises a substantial portion of a storm surge, sometimes reaching variations of the order of the meter.

1.4.3   Role of sea level rise

Human emissions of carbon dioxide and other greenhouse gases have been increasing exponentially since the industrial revolution (~ 1800). Although some steps have been taken to diminishing our contribution to ozone layer depletion and hence to the greenhouse effect and the consequent global warming, climate change effects are already present nowadays. Moreover, most experts point to an accelerated worsening of the conditions if immediate and drastic actions are not taken (Kopp *et al.*, 2014). In addition to altering climate at a global scale, which is already catastrophic on its own, global warming comes with the added menace of a considerable sea level rise, potentially reaching an increment of 1 meter by the end of this century, according to most estimates (Kopp *et al.*, 2014). This would suppose a threat not only to coastal settlements and their infrastructures but also to the local ecosystems and the species that inhabit them. Contrary to popular belief, the main reason for this rise is not only the increasing rates of glacial and ice sheets melting (which do also play an important part), but also the ocean thermal expansion. Some reports claim that around half of the sea-level rise over the past 25 years is attributable to warmer oceans simply occupying more space.

1.5   Previous works, aim and approach

This project is mostly inspired by Jaime Arriaga's doctoral thesis (Arriaga, 2017), where the Q2Dmorfo was adapted and successfully applied to model the long-term morphodynamic evolution of the Zandmotor (ZM) mega-nourishment, located on the Dutch Delfland coast. ZM is not the only site where the Q2Dmorfo has been used, but it is where the most extense study with this model has been made. Simultaneously to this TFG project, another one is carried out by my fellow Laura Portos in the ZM site including sea level variations and aiming to reproduce the response of the ZM site under different scenarios of sea level rise due to climate change. Sea level variations were neglected in the original thesis even knowing that only tides can already induce an overall effect up to a 15% change (Luijendijk *et al.*, 2017).

e **f**

The aim of this project is to characterise the morphodynamic evolution up to 2100 of the southern sector of the Llobregat delta under different climate change scenarios, including the sea level variability and the wave forcing. The model must be first validated in the study site and this is done with available data from 11 April 2012 to 11 April 2017, dates when LIDAR flights were made. Apart from the shorelines in these two dates, bathymetric information of the area is also available. Wave conditions in the domain boundaries had been propagated using the SWAN model before the start of this project and are available from 2010 until 2018. Sea level variations induced by astronomical, barometric and wind stress tides are assumed to be spatially uniform in the studied domain and its value in the validation period 2012-2017 has been obtained from the nearest sea level gauge, in Barcelona harbour.

These different data sets are described in detail in chapter 2, and the study site is characterised. Chapter 3 outlines the main components of the Q2Dmorfoorfo model. The wave setup, since it is spatially variable, has been included inside the model in the framework of the other TFG project by Laura Portos, and it is here also used. Chapter 4 includes the results of the model validation in the Llobregat delta site. The model is subsequently applied to simulate its morphodynamic evolution until 2100. Available studies show that wave conditions will not experience significant changes, existing models predicting them to be of the same order than the estimated errors. Thereby, the future wave conditions are constructed by repeating the conditions in the period 2012-2017. The decadal predictions of mean sea level rise due to global warming have been obtained through a collaboration of the Institut Mediterrani d'Estudis Avançats (IMEDEA, Mallorca) and come from the projections by Kopp *et al.* (2014). Different scenarios have been tested. These mean sea level projections are superimposed to a time series obtained by repeating the sea level variations of measured in Barcelona harbour from 2012 to 2017. The discussion and conclusions are reported in chapter 6.

2 Study site and data used

This section is devoted to explain and describe the characteristics and intricacies of the studied site, as well as to unravel and justify the treatment and filtering of the available data necessary to work with the Q2Dmorfo. The latter can basically be subdivided into: wave climate, sea level and topographic-related data.

2.1 Site description

The coast of the Llobregat delta, located west of the city of Barcelona, Catalonia, northeast of the Iberian peninsula, is divided from east to west by the municipal districts of el Prat de Llobregat, Viladecans, Gavà, Castelldefels and Sitges, in that specific order. For this project's sake the considered coast will be delimited by the breakwaters present in the Llobregat's mouth and the one covering Port Ginesta (upper right corner and bottom left of figure 2.1.1, respectively), both being excluded from the final domain. This election is by no means arbitrary, and responds to the need of simplifying the lateral boundary conditions imposed. As the considered domain rests between two large groins, it makes sense to assume that the transport in these lateral boundaries is negligible and can, therefore, be estimated as null (see section 3.4).

Figure 2.1.1: North-oriented satellite view of the southern sector of the Llobregat delta, Google Earth (2020)

The shoreline is characterized by a subtle curvilinear shape, that reaches its maximum convexity approximately halfway between the aforementioned extremes. Another distinctive trait of this coast is the large presence of ponds, creeks and pluvial/fluvial channels that traverse its beaches. As the Q2Dmorfo is not yet able to properly deal with these geographical features, they are removed from the initial topography, under the reasonable assumption that their contribution on the total sediment transport is negligible and that it will not affect the overall morphodynamic evolution of such a large coast. The same approach is applied to any groin or man-made structure within the shore studied. The sediment contribution of the Llobregat river is not taken into account either because the breakwater next to its mouth does extend to zones near the depth of closure, depriving most of the river-carried sediment to end in an active transport zone, meaning that it mostly dissipates slowly in the vicinity of the river's mouth, without affecting much the actual domain. Due to the fact that the wave shadow and diffraction produced by the delimiting breakwaters is not taken into account in the model, an exclusion zone will be set in both lateral boundaries, so that only the results in the areas that are truly unaffected by these processes are considered relevant and reliable. This is further discussed in chapter 4.

2.2   Wave climate data

The Llobregat delta coast, and in general all the Catalan littoral, is dominated basically by eastern, southeastern and southern waves[1]. However, the wave climate is not completely homogeneous all across the domain but changes along the coast due to the shoreline curvature (figure 2.1.1) (since waves tend to turn towards the shoreline), precluding the possibility of modelling the whole delta with an alongshore uniform set of wave conditions.
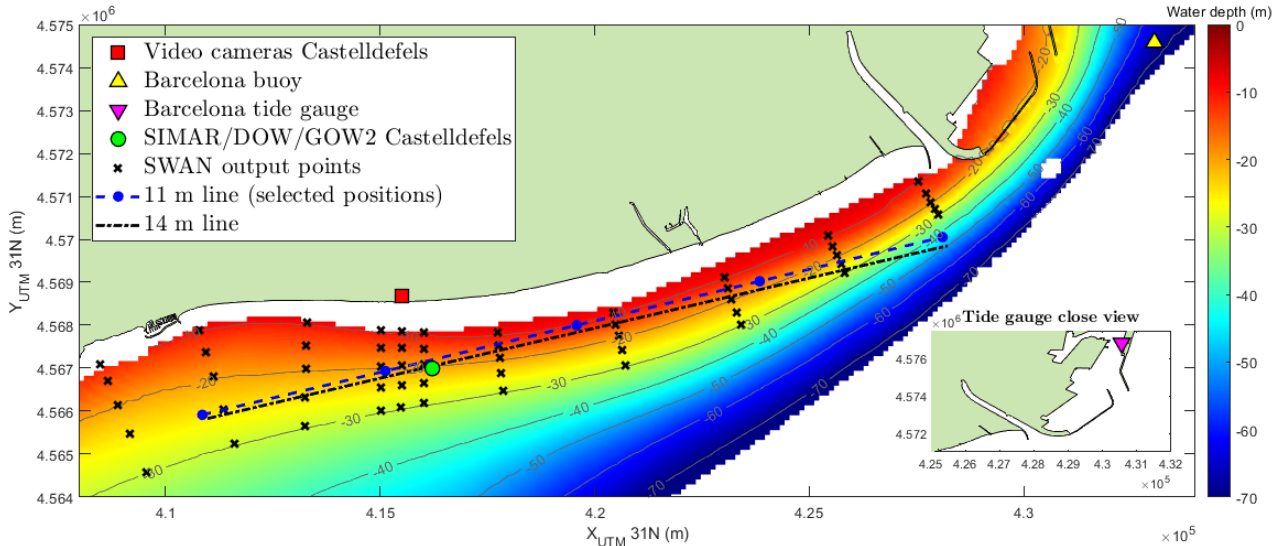

Figure 2.2.1: Llobregat delta bathymetry in UTM coordinates, including the position of multiple relevant data sources

Thereby in order to have a more faithful approach to the particular behaviour of the sub-zones within the considered domain, it was decided to use the wave data (composed of significant height, peak period and mean angular direction) from 5 roughly equidistant points within the so called 11 m line as Q2Dmorfo input. The aforementioned 11 m line (see figure 2.2.1) is an offshore imaginary segment in front of the Llobregat delta littoral with an angle (φ_{11m}) of $\sim$ 76.5° with respect to the North. It is important not to mistake the 11 m depth contour, which is isobathymetric, with the 11 m line, whose course goes through multiple profundities, raging between 40 and 11 m (the latter is named after the shallower depth included within its path). Both of its ends are chosen in such a way that if a perpendicular line to the segment was to be traced from there it would eventually intercede with the nearest delimiting breakwater.

The wave data along the 11 m line had been obtained by propagating the available hourly-recorded data of the Barcelona buoy (at 68 m depth, see its position in figure 2.2.1) to the selected positions. This propagation has been done before this project started using the Simulating WAves Nearshore (SWAN) model (Booij *et al.*, 1999), which is based on a fully spectral representation of the action balance equation. In broad terms, the model does formulate the wave evolution in terms of a spectral energy balance on a regular grid (or the action balance in the presence of ambient currents), with all physical processes (e.g. wind forcing) being modelled explicitly.

---

[1]Notice that, as it happens with winds, wave direction is described considering the direction they come from and not the one they travelling to.

Two types of simulations were carried out using the same initial data. These simulations just differed on boundary conditions of the propagated waves. While one made use of the measured 2D spectra, the other did only consider a set of integrated wave parameters (wave height, wave period, wave direction and directional spreading) previously stipulated within a so called TPAR file. When both outputs were available in the Barcelona buoy the 2D spectra approach was prioritised, since its boundary conditions are more restrictive and therefore, it guarantees a more realistic outcome. However, in some punctual occasions, due to the lack of 2D spectra in the buoy's measurements it was necessary to resort to the results attained with the TPAR simulation.
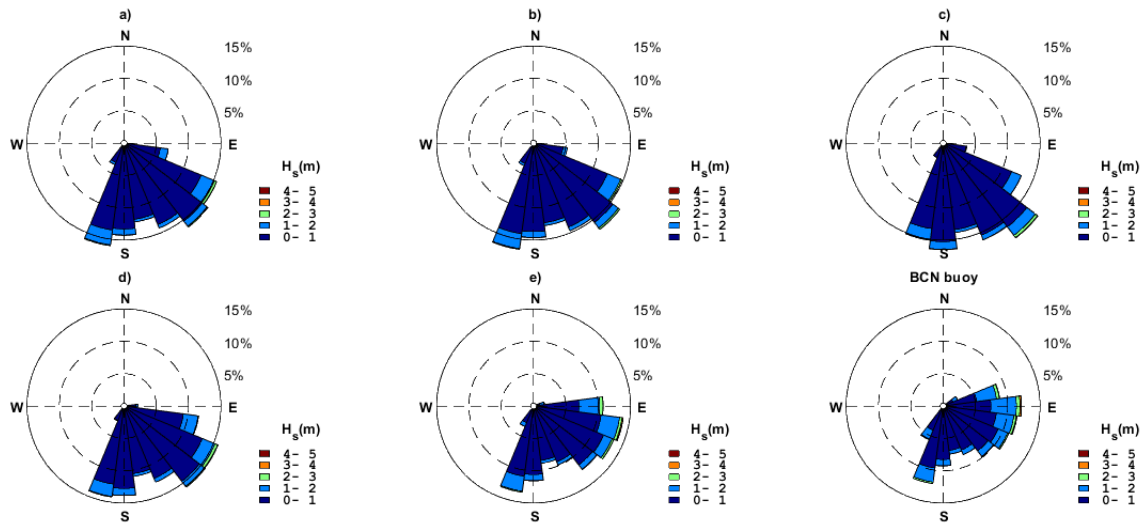

Figure 2.2.2: Wave roses indicating the incident direction and significant heights of waves between 2012 and 2018 in distinct points along the Llobregat delta coast, with a) to e) being 5 roughly equidistant positions, at different depths, along the 11 m line from west to east (see blue dashed line in figure 2.2.1)

Figure 2.2.2 shows the results of the wave propagation in the five points of the 11 m line, together with the original Barcelona buoy data. The significant height of the incident waves at the 11 m line rarely exceeds the 2 m mark, and its peak period oscillates around 4 s. Whilst the occidental front of the studied region is more prone to meridional and southeastern waves, the oriental side exhibits a climate more resemblant to the one observed in the Barcelona buoy, with a more prominent eastern component.

Combining both methods around a 96% of the hourly data necessary to cover the validation period (2012-2017) for each of the chosen points is obtained (with the 2D spectra simulations representing over a 92% of the total). The remaining 4% could not be propagated from the Barcelona buoy due to the absence of recorded measurements, caused either by equipment malfunctions or maintenance labors. In order to cover those gaps it was necessary to rely on the predictions of the meteorological model SIMAR, maintained by Puertos del Estado. SIMAR is a hindcast of wind, sea level and wave parameters for the entire Spanish coast that spans from 1958 until today. More specifically, the estimates retrieved from SIMAR's database were simulated for the output located in front of the Castelldefels coast (examine figure 2.2.1), at a sea depth of approximately 21 m. Since this output position is relatively nigh to the 11 m line, and keeping in mind that SIMAR's contribution to the overall validation period is not that remarkable, a simpler propagation method based on Snell's law of refraction (assuming rectilin-

ear and parallel depth contours) was applied. The results obtained for the propagated SIMAR data were satisfactory, even knowing the inherent uncertainty that working with this source of data entails (specially when regarding wave directions (Swart, Ribas *et al.*, 2020). A long gap (1 year) in the wave conditions in the Barcelona buoy occurred in 2009. Thereby, the model validation must start later than that.

2.3   Sea level data

Present days sea level data have been directly extracted from the hourly measurement record made by the tide gauge located within the port of Barcelona (REDMAR station nº 3758, latitude 41.34ºN longitude 2.17ºE, see figure 2.4.1). For the purpose of maintaining a uniform notation the NMMA zero reference has been taken, so any bed level or sea level in this project will be expressed with respect to this datum, unless specified otherwise. NMMA stands for 'Mean Sea Level in Alacant' and it it is a standard used state-wise to determine the ground zero from where most heights and profundities are calculated. Sea level variations in the Mediterranean are not specially pronounced, and for the chosen site during the validation period range between -0.18 and 0.52 m, with a mean level around 0.15 m (MSL), as shown in figure 2.3.1, where the evolution is slightly smoothed for representation purposes. Besides the transformation from the REDMAR zero reference to NMMA, the data retrieved from the tide gauge need no additional filtering. Even though some hourly gaps do exist during the validation period, the model already does replenish them doing a linear interpolation between the two closest available times.
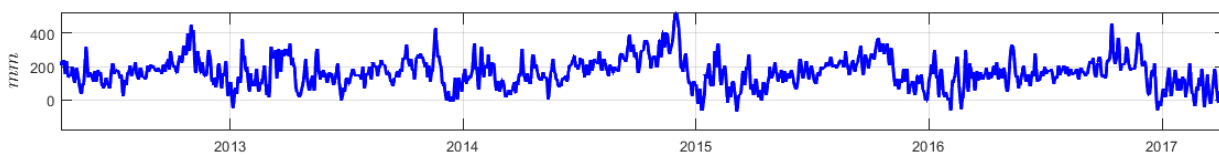

Figure 2.3.1: Sea level time series during the validation period (slightly smoothed)

Most of the modelled global predictions of the sea level rise struggle to represent its evolution in the Mediterranean sea, since they are unable to characterise the water exchanges in the strait of Gibraltar. There exists some local models specific for the Mediterranean but none of them has been recently updated to include the most recent climate change predictions. Moreover, these regional estimations also depend on an ensemble of global forecasts to function properly, further hindering their implementation. Ultimately, it was here decided to rely on the predictions for the closest available point in the Atlantic ocean, under the assumption that for large scales of time the regional influence over sea level diminishes in front of the global tends. In consequence, the projections for sea level rise used in this project come from the computations made by Kopp *et al.* (2014) for the Lagos tide-gauge, located in the region of the Algarve, in southern Portugal. This site is to be used as a proxy for the Mediterranean.

In Kopp *et al.* (2014) three main scenarios (extracted from Meinshausen *et al.*, 2011) are examined: RCP2.6, RCP4.5 and RCP8.5, which correspond respectively to likely global mean temperature increases in 2081–2100 of 1.9–2.3 ºC, 2.0–3.6 ºC, and 3.2–5.4 ºC above 1850–1900 levels (Intergovernmental Panel on Climate Change, IPCC, 2013). Again, RCP stands for Representative Concentration Pathway, and each of the attached numbers makes reference to a different prognostic for anthropogenic emissions of greenhouse gases. For instance, RCP2.6 represents the improbable event of a strong mitigation of emissions during the forthcoming years, whereas RCP8.5 can be viewed as corresponding to high-end business-as-usual evolution of emissions, making it the most likely scenario between the three pathways. RCP4.5 stands halfway, as a

moderate mitigation situation. From each of these global warming scenarios Kopp *et al.*, (2014) were able to obtain a range of sea level projections. These estimates account for all the factors and spatiotemporal variations related to sea level, that is thermal expansion (also associated to oceanic currents), the contribution of melting glaciers and polar ice caps, changes in Earth's hidrostatic reservoirs, glacial isostatic adjustment (ongoing movement of land once burdened by ice-age glaciers) and the effects of mass redistribution on the planet's surface.

To fully adapt each scenario to the Llobregat delta, the geologic evolution of the site has also to be taken into consideration. Most delta plains suffer from subsidence, the gradual downward settling of the seabed, and our case is not an exception. A preliminary satellite study carried in 2004 claims that the delta sinks at a rate between 0.5-1 cm/year (Duro *et al.*, 2004). Since this effect must be modelled as a sea level rise of the same magnitude, the aforementioned rates would imply a MSL increase of at least 450 mm by 2100, if only subsidence was accounted. Nonetheless, it was finally decided to opt for a more conservative rate of 1.5 mm/year, widely regarded as a general mean subsidence rate for deltas (Bianchi, 2016).

2.4 Bathymetric data

Three main sources of bathymetric information are to be differentiated: the LIDAR (Laser Imaging, Detection and Raging) data of beach topography (that from now on will be simply referred as LIDAR), the deep bathymetric data and the time-averaged Castelldefels beach profile. However, before detailing each of these measurements, it is precise to properly define the domain using a rectangle that suits Q2Dmorfo requisites. To understand the criteria used to choose the rectangle perimeter, it is necessary to explain how the data in UTM coordinates must be rotated into a new axes $\{x, y\}$ that fits the model framework. The cited transformation obeys the following equations:

$$x = a + X_{UTM} \cos\theta + Y_{UTM} \sin\theta \quad , \quad y = b - X_{UTM} \sin\theta + Y_{UTM} \cos\theta \tag{2.1}$$

where $\{a, b\}$ values are determined by the election of a suitable $\{X, Y\}_{UTM}$ coordinates for the rotation point (one of the vertices of the rectangle), that once the transformation will be applied will also become the origin of the new system of reference $\{x, y\}$ (see figure 2.4.1). The Q2Dmorfo works under the implicit assumption that the x axis is nearly perpendicular to the mean orientation of the shoreline and points seaward. Thus, in our case, the x axis is parallel to the short laterals of the rectangle and points seaward, whilst the y coordinate is aligned with the long side of the rectangular domain and points to the East. Furthermore, the z axis must point upward, to complete a right-handed system of Cartesian coordinates. The θ parameter in equation (2.1) indicates the rotation angle.

The 11 m line is taken as the long offshore side of the rectangle, under the educated guess that the depth of closure (D_c) is situated far shoreward of the 11 m depth contour meaning that any sediment transport beyond this limit is negligible. From this election, one can already reckon that the angle θ has to be $360^o - \varphi_{11m} \simeq 283.5^o$. Then, the opposite side is chosen to guarantee that, once the domain is rotated, there will be at least a 200 m strip of dry beach behind the shoreline. To do so, the seaward limit of the LIDAR was translated 200 m inland in the direction perpendicular to the 11 m line. Next, the long northernmost side was constrained to intersect with the minimum of the translated curve, that can be easily determined by rotating it an angle θ, leaving a domain of dimensions $\{2627.5 \times 17675\}$ m, with a total area of $\sim$4645ha. The values that arise for a and b are 4346585.7 and -1465063.3 m, and the rotated domain is shown in figure 2.4.2a.

Laser Imaging, Detection and Raging (LIDAR) is an optical technique used to measure the distance from an emission point to a target by illuminating the latter with laser light and measuring its reflection with a sensor. This method has been used to measure the topography of Llobregat delta beaches down to a height of $z_b = 0.38\ m$ in multiple occasions. LIDAR data is obtained through a collaboration with researchers of the Marine Research Institute (ICM, CSIC, Barcelona). The landward end of the LIDAR marks the end of the beach and the beginning of urbanized/metropolitan zones, infrastructures or other ecosystems. This frontier will play an important role later on to compute the loss of beach area due to the sea level rise and to determine the effects of floods. The LIDAR employed to reconstruct the initial bathymetry was carried out on 11 April 2012. This is the first LIDAR available from 2010 (so in the period with good wave conditions) and it is followed by yearly LIDARSs during 5 years. Thereby, it defines the beginning of the validation period. It is worth mentioning, once again, that some filtering of 2012 LIDAR was necessary in order to erase several geographic features such as creeks, channels or ponds, as well as some man-made structures, e.g. groins. In most of the cases a simple surface interpolation using the remaining data was sufficient to recreate a refined version of the dry beach.
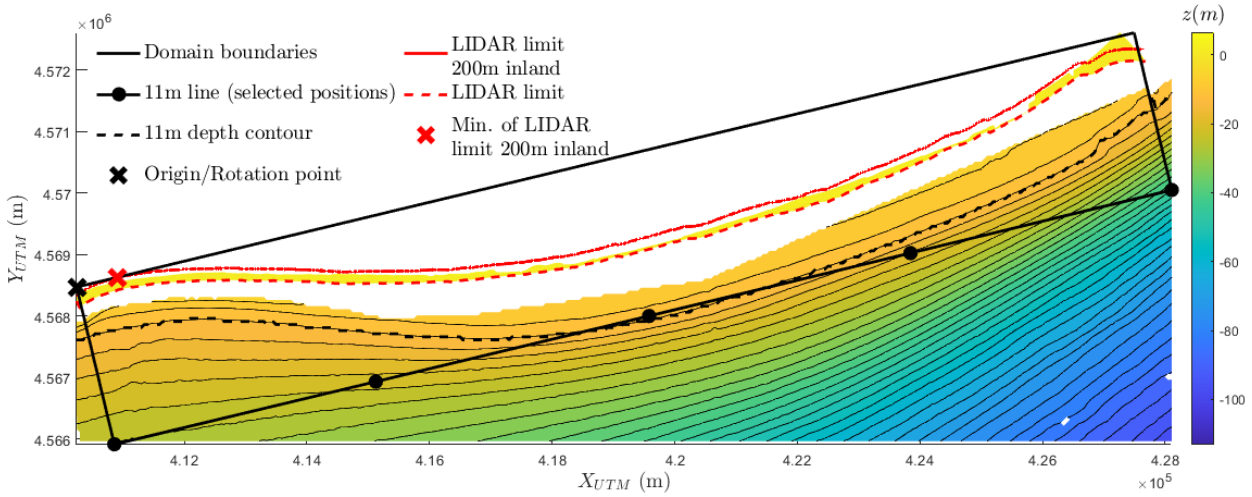

Figure 2.4.1: LIDAR and deep bathymetry data in UTM coordinates with the different limits. The rectangle domain is also shown.

A deep bathymetry of the central Catalan coast is also available through the researchers of the ICM. However, as can be seen in figure 2.4.1, there is an important gap between the LIDAR data shoreward end and the shoreward boundary of the deep bathymetry. The lack of data in this nearshore zone leaves no alternative but to rebuild this part of the bathymetry with the only source of information available, that is a Castelldefels time-averaged beach profile (red line in figure 2.4.2c). This profile had been previously obtained by performing a time- and alongshore-average of about 12 bathymetries measured yearly in front of Castelldefels area from 2011 until 2019 (in an horizontal area of 1 km^2 approximately). The idea behind this procedure is to replicate the beach profile measured in front of Castelldefels along the whole domain. An equilibrium profile z_{be} of the site is also needed, and it will be assumed to be proportional to the Castelldefels beach profile, z_{cdf}, for that $z_{be} = f_{eq}z_{cdf}$, where f_{eq} is a factor to be adjusted during validation.

The procedure to refill the bathymetry starts by establishing that the deep bathymetry is used only for $z_b \leq -11\ m$ (dashed black line in figure 2.4.1). Then, the available Castelldefels profile

must be matched both to the LIDAR (at $z_b = 0.38\ m$) and to the deep bathymetry (at $z_b = -11$ m), imposing continuity. Thus, only the fragment of Castelldefels profile that goes from the MSL to a depth of 6 m is used. The remaining empty domain is composed of two stripes, that is from a 6 to 11 m depth and from MSL to $z_b = 0.38\ m$. They are filled using two linear regressions that serve as a junction between the cropped profile end and the deep bathymetry for the former, and between the cropped profile start and the LIDAR for the latter (figure 2.4.2c). Please Notice that in this graphic the proportion between axes x' and z is 10 to 1, so the Castelldefels beach profile splice to the actual bathymetry is not as abrupt as it may appear. Also, $x'(y) = x - x_{MSL}(y)$, with $x'_{MSL}(y)$ being a function depending on y that determines the cross-shore position for which $z_b = \text{MSL}$.

Finally, the hollow space behind the LIDAR must also be defined. This region does not actually belong to the Llobregat delta beach so there is no manner of rebuilding it, instead a flatland is designed to cover the vacant domain. We do it by extending landward each of the points within the LIDAR onshore limit until reaching $x = 0$, forming a kind of more or less uniform plain that extends all across the beach topography. After all the mentioned processing, the resulting initial bathymetry is depicted in figure 2.4.2b.
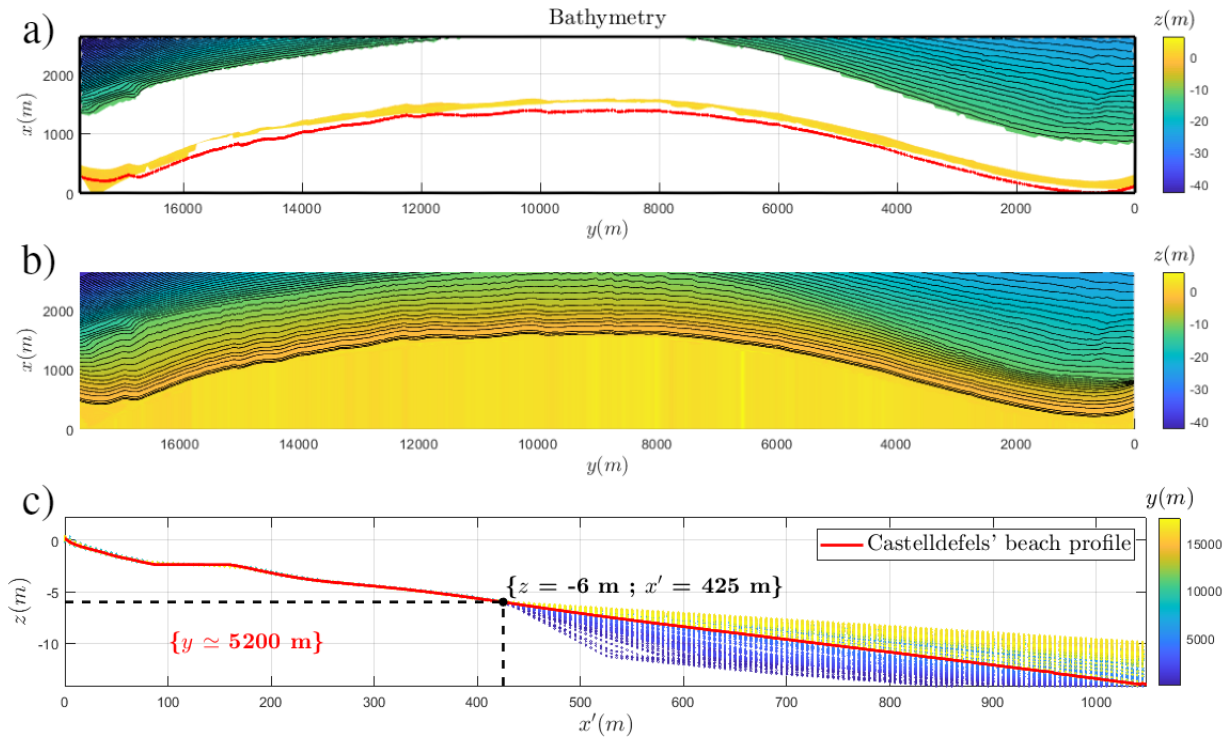

Figure 2.4.2: (a) LIDAR and deep bathymetry in the rotated final domain and (b) reconstructed bathymetry. Notice that the y axis points towards the left. (c) Aligned representation of the reconstructed cross-shore beach profiles for different values of y

2.5   Coastlines

LIDAR data were available every year from 2012 to 2017 and this is why this period is chosen for validation. From each of these LIDAR a reference coastline had been extracted for the $z_b = 0.38$ isobathymetric line. These reference shorelines are used during the validation process, to determine the accuracy of the modelled results. Firstly, we validate the reconstructed initial bathymetry by comparing the reference coastline that can be obtained from there with the one

from 2012 LIDAR. This comparison is illustrated in figure 2.5.1a and, as one can appreciate, there is not a discernible difference between both. This implies that the reconstructed initial bathymetry is consistent with the real shoreline despite the modifications introduced.

An analysis of the rest of the shorelines (2013-2017) is also worthwhile. In figure 2.5.1b the difference between the 2012 LIDAR reference shoreline and the ones obtained from these years is shown. Little evolution can be observed, and the most significant changes do not follow an erosion/accretion pattern but there is a back and forth time oscillation in some points (e.g. $y \simeq \{0, 6000, 10000, 17000\}\ m$). So, one can already perceive that the modelled shoreline changes in these 5 years will have to be really small in order to match the data.
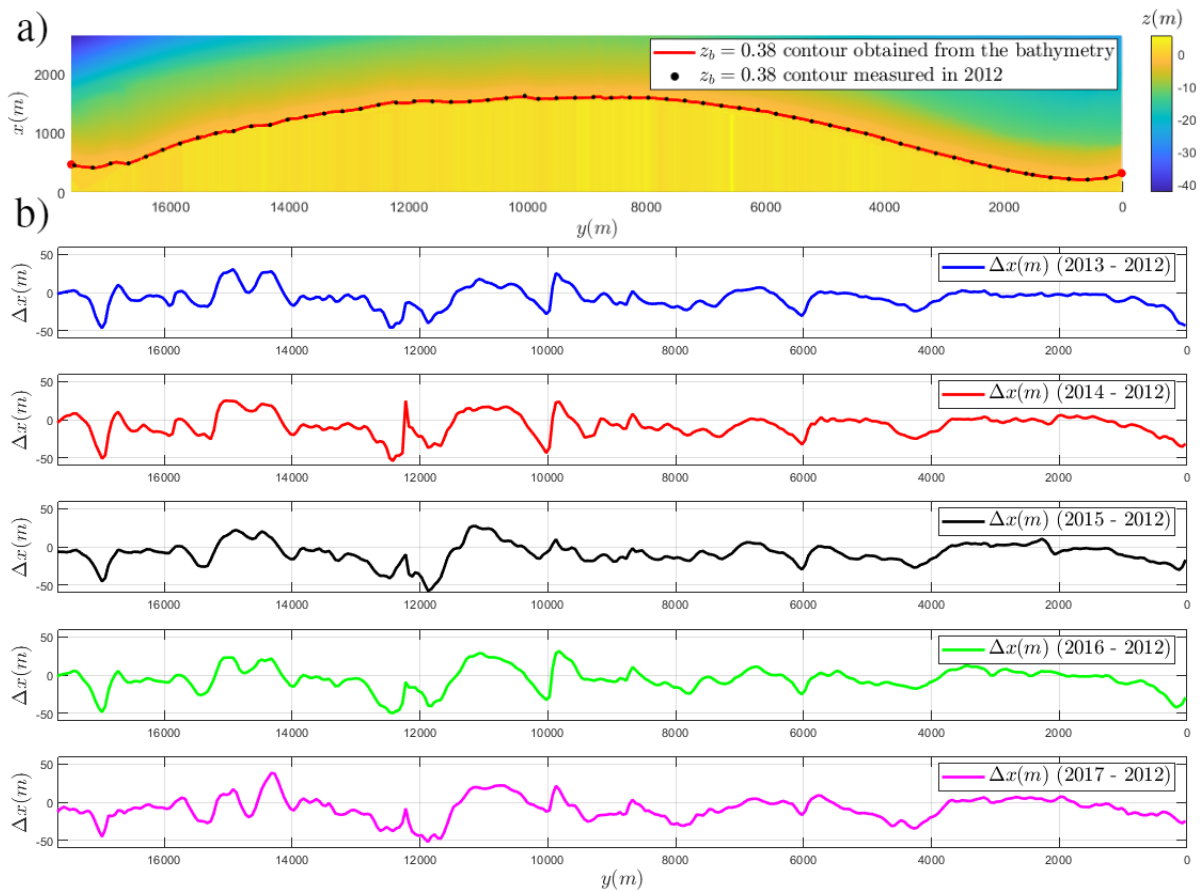

Figure 2.5.1: (a) Comparison between the depth contour at $z_b = 0.38\ m$ obtained from the LIDAR and from the reconstructed initial bathymetry. (b) Cross-shore difference (Δx) between the LIDAR shoreline in each of the years during the validation period, excluding the first (2013-2017), and the one in 2012.

3 Q2D-*morfo* model

The Q2Dmorfo model is described in detail because in this application to the Llobregat delta several internal parameters have been adjusted. More details of the model formulation can be found in Arriaga (2017).

3.1 Model domain and reference systems

The Q2Dmorfo works with a Cartesian frame of reference $\{x, y\}$, already introduced in section 2.4, where the y axis crosses the southern sector of the Llobregat delta, from port Ginesta to the river mouth, being approximately parallel to the mean shoreline; whilst the x direction (perpendicular to y) points offshore. The domain is comprised within a rectangle defined by the limits: $0 < x < L_x$ and $0 < y < L_y$, where L_x and L_y are the cross-shore and alongshore domain lengths, respectively. These longitudes take the following values: $L_x = 2630\,m$ and $L_y = 17700\,m$, so $L_y >> L_x$. The x axis points southeast, at an angle 76.5^o from North in the clockwise direction.

Within the rectangular domain two grids are defined (figure 3.1.1a): main one (solid lines) and the staggered grid (dashed lines). Notice that whilst the staggered grid is formed by $\{n \times m\}$ intersections (numbered as $\{i_c, j_c\} = 1, ..., \{n, m\}$), the geometric grid has $\{(n+1) \times (m+1)\}$ points since its indices $\{i, j\}$ include position zero. Each grid is just an spatial translation of the other, equal to $\Delta x / 2$ in the x-axis and $\Delta y / 2$ in the y-axis, with Δx and Δy being the cell grid size in the x and y directions. Since the ratio $\Delta x / \Delta y$ has to remain below 0.25 to prevent the wave rays to exit the grid cells through its lateral boundaries during wave transformation (for wave direction at the offshore boundary (θ_0) under 89° with respect to the y axis) (Arriaga, 2017), Δx and Δy are taken equal to 5 and 50 m, respectively. It can be easily determined that $n = 526$ and $m = 354$. Far more resolution is given to the x coordinate than to the y axis. This comes as a consequence of the complexity that involves the cross-shore dynamics.
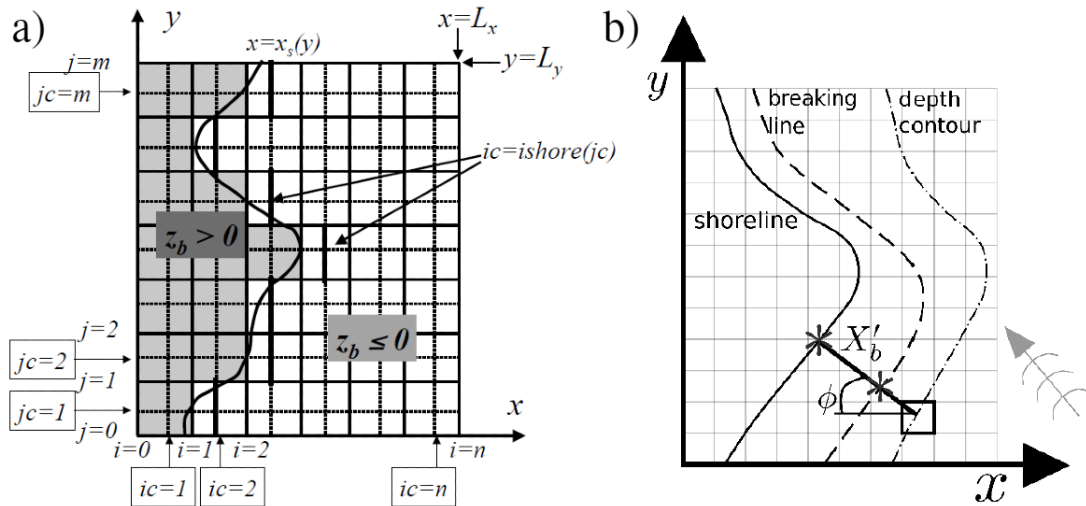

Figure 3.1.1: a) Geometry of the model domain and the staggered grid. b) Local cross-shore direction and scheme of ϕ and X'_b. Extracted from Arriaga (2017).

The model characterises the shoreline position, $x_s(y, t)$, as the separation between the wet cells ($D \geq 0$) and the dry ones ($D < 0$). Here, D represents the modelled depth and is computed as $\eta - z_b$. Nevertheless, the grid-based approach only allows to obtain a discrete x_s. To attain a better estimate of its position amidst the cells of the staggered grid for a certain y, an interpolation is conducted between the last wet cell and the first dry one. The resulting $x_s(y, t)$ is assumed to be an uni-valued function, so the model is not able to deal with the dynamics of, e.g., sand spits.

3.2 Modelling sediment dynamics and bed evolution

The changes in the bed level are computed with the sediment mass conservation, which is solved throughout the whole domain for every time step and can be expressed as follows:

$$\frac{\partial z_b}{\partial t} + \frac{\partial q_x}{\partial x} + \frac{\partial q_y}{\partial y} = 0 \tag{3.1}$$

where t is the time, $\vec{q} = (q_x, qy)$ the depth-integrated sediment flux in $m^3/(m \cdot s)$, and z_b is the bed level. The z_b initial value is read from an external file that is previously elaborated following the procedure explained in section 2.4. In regard to the numerical implementation, equation (3.1) is discretised using an explicit second order Adam-Bashford scheme in time and a standard finite difference in space (Berg, 2012).

To be able to calculate the evolution of the sea bed using equation (3.1), it is first necessary compute the depth integrated flux for each instant of simulated time. The model decomposes $\vec{q}$ in three terms:

$$\vec{q} = \vec{q_L} + \vec{q_N} + \vec{q_D} \tag{3.2}$$

In the forthcoming paragraphs the computation of each of the components is discussed.

An important feature of the Q2Dmorfo model is that it accounts for the local cross-shore and alongshore directions in order to compute the corresponding cross-shore and longshore transport more accurately. The local cross-shore direction is defined for every grid point by taking into consideration the neighbouring depth contours (see figure 3.1.1b). The mean angle between the normal direction of the associated isobathymetric and the x coordinate is obtained employing:

$$\sin \phi = \frac{\frac{\partial \overline{z}_b}{\partial y}}{\sqrt{\left(\frac{\partial \overline{z}_b}{\partial x}\right)^2 + \left(\frac{\partial \overline{z}_b}{\partial y}\right)^2}} \tag{3.3}$$

where the sea bed $\overline{z}_b$ has been spatially averaged within a rectangular box $\{L_l \times L_c\}$. The shoreline angle, ϕ_s, is also computed with equation (3.3) but the cells of the rectangular box with $z_b > 0$ are not included into the averaging, to exclude the influence of the dry beach. The normal and tangential unitary vectors that arise from a certain angle ϕ can be written as $\hat{n} = (\cos \phi, -sin\phi)$ and $\hat{t} = (\sin \phi, \cos \phi)$. This method allows the model to deal efficiently with sharply curved beaches.

The first term in equation (3.2) is the longshore littoral drift ($\vec{q_L}$) driven by the momentum and energy transferred during wave breaking. In order to estimate it, the total sediment transport rate (Q) is first computed using the CERC formula (Komar, 1998):

$$Q(y') = \mu H_b^{5/2} \sin\left(2\alpha_b\right), \quad \text{with} \quad \alpha_b = \theta_b - \phi_s \tag{3.4}$$

ef

Here, H_b and θ_b are the root mean square wave height and the wave front mean direction, respectively, at the breaking line, whereas ϕ_s represents the angle between the x-axis and the coastline. The variables H_b and θ_b depend on y' because the bathymetry changes in the alongshore direction. The constant μ in equation (3.4) is given by the original CERC expression:

$$\mu = \frac{K}{16(s-1)(1-p)} \sqrt{\frac{g}{\gamma_b}} \tag{3.5}$$

with s, p and γ_b being the relative density, porosity of sediment and wave-breaking saturation ratio, respectively. Standard values for these parameters are: $s = 2.65$, $p = 0.4$ and $\gamma_b = 0.5$. Given the values $K \sim 0.2 - 1.6$ suggested in Komar (1998), a range $\mu \sim 0.06 - 0.45\, m^{1/2}s^{-1}$ is obtained. However, this consists only of a rough estimate and other sources allude to smaller values of μ, e.g. $\mu \sim 0.012 - 0.15\, m^{1/2}s^{-1}$ (Wang & Kraus, 1999), thereby, μ needs to be calibrated in the study site. Once chosen a suitable μ and computed the total sediment transport alongshore, it has to be redistributed across the profile. This cross-shore distribution is assumed to be similar to the one of an alongshore current profile, using a normalized shape function (Komar, 1998):

$$f(x') = \frac{4x'^2}{\sqrt{\pi}L^3} e^{-(x'/L)^2} \tag{3.6}$$

where x' (local cross-shore direction) represents the distance to the shoreline and $L = 0.7X_b' + X_{sz}'$. Here, X_b' is the width of the surf zone (from the breaking line to the shoreline, see figure 3.1.1b) and X_{sz}' parametrises the width of the swash area (region affected by wave sway, see figure 3.2.1). These lengths, along with the x' coordinate, are determined in the local normal direction, using the corresponding angle ϕ (figure 3.1.1b). Lastly, the littoral drift is defined as the product of both magnitudes (equation 3.4 and equation 3.6), and is imposed to be tangent to the local bathymetric contours:

$$\vec{q_L} = Q(y')f(x')\hat{t} \tag{3.7}$$

The second term in equation (3.1), parametrises the cross-shore sediment transport that tends to drive the instantaneous profile towards a predetermined monotonic equilibrium profile (z_{be}). The assumption of the existence of such equilibrium profile is one of the distinctive traits of the Q2Dmorfo. In the present application, z_{be} is read from an external file, which is previously elaborated as explained in section 2.4. Then, $\vec{q_N}$ reads:

$$\vec{q_N} = -\gamma_N(\nabla z_b \cdot \hat{n} + \beta_e)\hat{n} \tag{3.8}$$

As shown, $\vec{q_N}$ is proportional to the difference between the equilibrium slope (β_e), at local depth D, and the actual bathymetric slant in the direction perpendicular to the local shoreline ($\nabla z_b \cdot \hat{n}$). The factor γ_N is the cross-shore diffusivity, associated to the impact that turbulence and orbital velocities from incoming waves have on the sea floor, and can be evaluated by means of:

$$\gamma_N(x) = \nu_N \gamma_b^{-1/6} H_b^{11/6} X_b^{-1/3} \psi(x) \tag{3.9}$$

This expression comes from an estimate of the momentum mixing (Battjes, 1975) that has been subsequently scaled with a power of H_b, the wave height at the breaking line. The non-dimensional parameter ν_N must be calibrated. The function $\psi(x)$ moulds γ_N all across the bathymetry and it has a maximum at the shoreline. From there, its value decays in both the onshore and the offshore directions, as:

$$\psi(x) = \left(-\left(\frac{x-x_s}{X_{sz}}\right)^4\right), \qquad \psi(D) = \frac{1+b+\tanh\left((\alpha D_c + z_b)/L_d\right)}{1+b+\tanh\left(\alpha D_c/L_d\right)} \tag{3.10}$$

where equation (3.10a) is applied to the domain dry cells and equation (3.10b) to the wet ones (figure 3.2.1). In the first expression $\psi(x)$ drops from one to zero in a distance controlled by the parametrised width of the swash zone, X_{sz}, whilst $x - x_s$ computes the distance to the coastline. In all the wet cells, the function does also start being equal to one at the shoreline, in order to guarantee its continuity, and decreases offshore to a small prescribed value at the closure depth, $\psi(D_c) = f$. The value of b can be determined as a function of f ($b \simeq 2f/(2-f)$). The model instantaneous depth of closure (D_c) is estimated as a fraction of the depth in which the first numerically appreciable sediment transport occurs (D_m). Hence, $D_c = f_c D_m$, where constant f_c has to be calibrated. The residual value of the function for large profundities is $\psi(\infty) \simeq f/2$, whereas the decay rate is modulated by α, since L_d is set to $0.5\alpha D_c$. The values used in previous applications were $f = 0.02$ and $\alpha = 0.406$; nonetheless, during this project it was necessary, after the initial tests were carried, to fix them at $f = 0.002$ and $\alpha = 0.502$, to favor cross-shore sediment transport in shallower waters and to preserve the deep bathymetry.
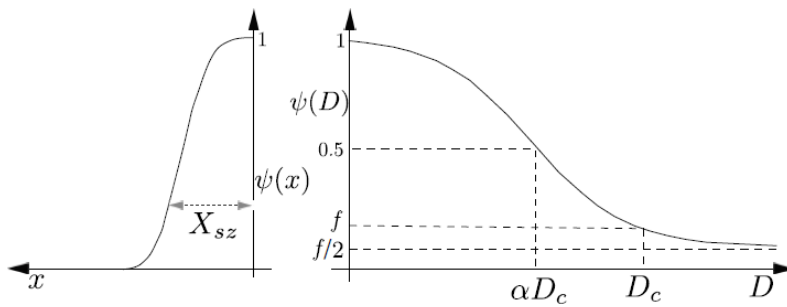

Figure 3.2.1: Cross-shore distribution of the ψ function. Extracted from Arriaga (2017).

Finally, the third term in equation (3.2) is an alongshore diffusive transport that reproduces the smoothing tendency of small sandbars or bumps due to the action of wave breaking. This flux does also serve as a numerical stabilizer that prevents small-scale morphodynamic noise. For the applications meant during this project, the diffusivity factor γ_D will be taken equal to γ_N, so $\vec{q_D}$ equals:

$$\vec{q_D} = -\gamma_N (\nabla z_b \cdot \hat{t})\hat{t} \tag{3.11}$$

From the previous description of the sediment transport, notice that the swash zone, located in the surroundings of the shoreline, is treated as a transition region. This essentially implies that all variables and functions described are set, or enforced, to change smoothly from the values corresponding to the wet cells to those of the dry ones. This method has been baptised as the 'fuzzy shoreline' approach.

Before concluding this section, it is worth mentioning a new feature that has been successfully introduced to the Q2Dmorfo during the course of this project. It consists on the establishment of an inactive zone within which transport sediment will not be computed. The idea behind this is to save simulation time by avoiding the update of the topography of the region on the beach backshore, which is not actually relevant to the morphodynamic evolution of the rest of the domain. In the case of the Llobregat delta the inactive zone has been defined as the parabolic approximation ($F(y) = ay^2 + by + c$, for $F(y) > 0$) of the LIDAR land limit displaced 200 m inland (with $a = -2.16 \cdot 10^{-5}$, $b = 0.42$ and $c = -625.19$, see figure 3.2.2). Furthermore, in the present application case this area is nothing but an artificial flatland designed to cover the onshore end of the topography, which reinforces the convenience of defining it as an inactive zone.
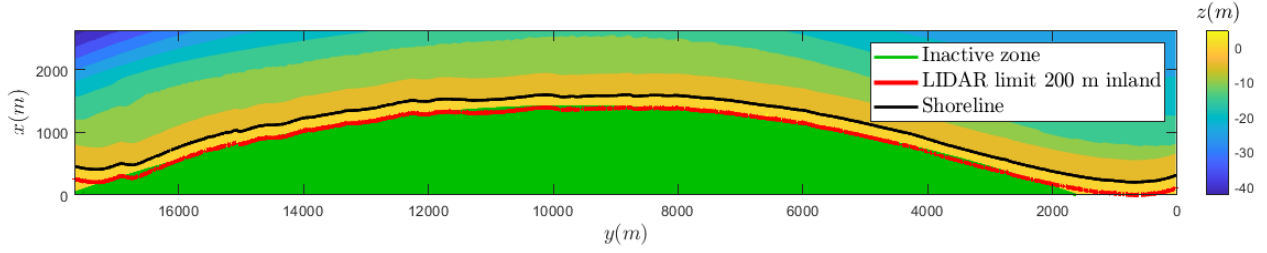
e **f**

Figure 3.2.2: Inactive zone applied in the Llobregat delta application.

3.3 Modelling wave transformation

The Q2Dmorfo wave transformation approach takes into consideration the processes of refraction and shoaling over the curvilinear depth contours by assuming monochromatic waves with root mean square height (H), peak period (T) and mean direction angle θ. These magnitudes are propagated from the offshore boundary ($x = L_x$) with an initial value of $\{H_0, T_0, \theta_0\}$. To do so, three decoupled equations, i.e. the dispersion relation, the wave number irrotationality and the wave energy balance:

$$\omega^2 = gk \tanh kD \tag{3.12}$$

$$\frac{\partial k_y}{\partial x} = \frac{\partial k_x}{\partial y} \tag{3.13}$$

$$\frac{\partial}{\partial x}\left(c_g H^2 \frac{k_x}{k}\right) + \frac{\partial}{\partial y}\left(c_g H^2 \frac{k_y}{k}\right) = 0 \tag{3.14}$$

are solved numerically following this specific order. Both wave diffraction effects and bottom shear stresses are disregarded, and steady conditions are assumed. From the resulting modelled wave field H_b and θ_b, the wave height and direction at the breaking point, can be obtained and subsequently used in the already described sediment transport equations. In order to do so, the breaking point is defined as the most onshore position for which $H \leq \gamma_b D$ is satisfied. The model does not scan throughout the whole domain to identify the breaking point, but a parameter f_1 is defined. So that only positions where $D \leq f_1 D_{bm}$ are inspected, with D_{bm} being the maximum breaking depth found in the previous iteration.

Since the sea bed evolution is much more slower than the wave field changes, there is no need of computing the latter for every time step Δt, but instead it is updated every $\Delta t_w = N\Delta t$. In previous model applications it was found that using a $\Delta t_w = 100\Delta t = 0.1$ days did not affect the morphological evolution. The same value of Δt_w will be adopted for the Llobregat delta simulations. To evaluate the offshore wave conditions at the needed discretised times, which do not coincide with the measurement times, a linear regression is performed between the two temporally nearest measurements.

Before this project started, the model was only able to work with alongshore-uniform wave conditions offshore, so that the measurements retrieved for a chosen buoy had to be assimilated by all grid points of the offshore boundary. In other words, the wave conditions $\{H_0, T_0, \theta_0\}$ at $x = L_x$ for every time step (Δt_w) were the same for each y position considered. This approach is reasonable when modelling sites where the deep bathymetric contours are nearly parallel to the y-axis, since the seaward border can be approximated to an isobathymetric line within which the wave climate does not vary much. However, this is not the case for the $11\,m$ line in the Llobregat delta, where profundities range between 11 and $40\,m$. Hence, the Q2Dmorfo has been extended to read multiple input files, each including the wave data of a certain position of the

offshore boundary. For example, in the present case five roughly equidistant points belonging to the 11 m line are selected (see section 2.2). Then, for every y position an interpolation process is performed between the two closest data sources, so as to determine the wave magnitudes that are to be propagated towards the shore. Notice that this process has to be carried once the temporal regression is completed. Before this propagation takes place a further restriction over θ_0 is imposed: it can not be greater than 80º, measured with respect to the normal direction of the neighbouring depth contour of each position in the offshore boundary. This additional constraint is established to avoid wave rays exiting by the lateral boundaries of the grid cells in cases with sharply curvilinear isobathymetric lines.

Another important recent change in the model was the implementation of the effect of wave set up, using the following formula:

$$z_{s_{wsu}}(x,y) = \frac{3\gamma_b^2}{8 + 3\gamma_b^2}[D(x_b(y),y) - D(x,y)] \quad \rightarrow \quad \eta = z_s + z_{s_{wsu}} \tag{3.15}$$

where x_b is the x-coordinate of the breaking point for a specific value of y, z_s the hourly sea level measurements of the studied site that are introduced to the model, η the resulting sea surface, and $z_{s_{wsu}}$ the sea level variation due to wave set up. This improvement came as a result of a TFG that was made in parallel to this one: *"Effect of sea level variations in the long-term dynamics of the Zandmotor meganourishment"* (Portos, 2020).

3.4 Boundary conditions and numerical discretisation

The Q2Dmorfo offers a variety of options for the boundary conditions of z_b: closed system (no sediment transport), linear extrapolation (relaxation towards equilibrium) or Dirichlet constraints. It also differentiates between the conditions imposed on the offshore limit and the ones on the lateral boundaries, which can be chosen separately, hence allowing combinations of the previous choices. For the purpose of this project only one option will be described, that is the closed domain case. This is the simplest condition since it only consists in imposing null sediment transport ($q = 0$) at positions where $y = 0$, $y = L_y$ or $x = L_x$, meaning that the quantity of sediment will be conserved throughout time (no sand is able to leave the domain). The only requirement needed for this treatment to be reasonable is that the sediment flux significantly decays offshore, until reaching almost negligible values, and it is null in the lateral boundaries. This is definitely fulfilled in the Llobregat delta case, as it has been stated before, since on the one hand the transport in the lateral boundaries is blocked by the delimiting breakwaters and, on the other hand, the offshore limit is situated well beyond the expected depth of closure, making the transport there irrelevant. As for waves, the wave sheltering and wave diffraction for the breakwaters at both lateral boundaries are not accounted for in the model.

To guarantee numerical stability the time step Δt (in days) must be chosen in accordance with the Courant condition:

$$\Delta t < 1.5 \cdot 10^{-6} \cdot \frac{H_0^{3/2}\min(\Delta x, \Delta y)^2}{\nu} \tag{3.16}$$

This expression is found using the diffusivity given by equation 3.9. The value finally chosen for Δt is 0.001 days, based on the one used in the ZM simulations. This value satisfies inequation (3.16), with some margin to adjust ν.

e^f

4 Model validation

In this section the process of validation of the Q2Dmorfo with data of the Llobregat delta from 2012 to 2017 is described. It consists on selecting the parameter values that provide shorelines as similar as possible to the real measured shorelines. However, before that, some preliminary tests are explained that allow to solve a problem encountered when applying the model to this site, with the appearance of a persistent numerical instability.

4.1 Numerical instability

Before starting with the actual process of validation some previous tests have been carried out for the Llobregat delta site during the validation period (April 2012 - April 2017). To do so, the parameters fitted for the ZM simulations, i.e. $\nu = 0.05$, $\mu = 0.04 \, m^{1/2}s^{-1}$, $f_1 = 2$, $f_c = 0.15$, $X_{sz} = 10 \, m$ (Arriaga, 2017), are adopted. The main purpose of these simulations is establishing a fixed value for the factor f_{eq}. This parameter has a strong impact on the final results, since it modifies the equilibrium profile, which in turn plays a crucial role when modelling the cross-shore transport.
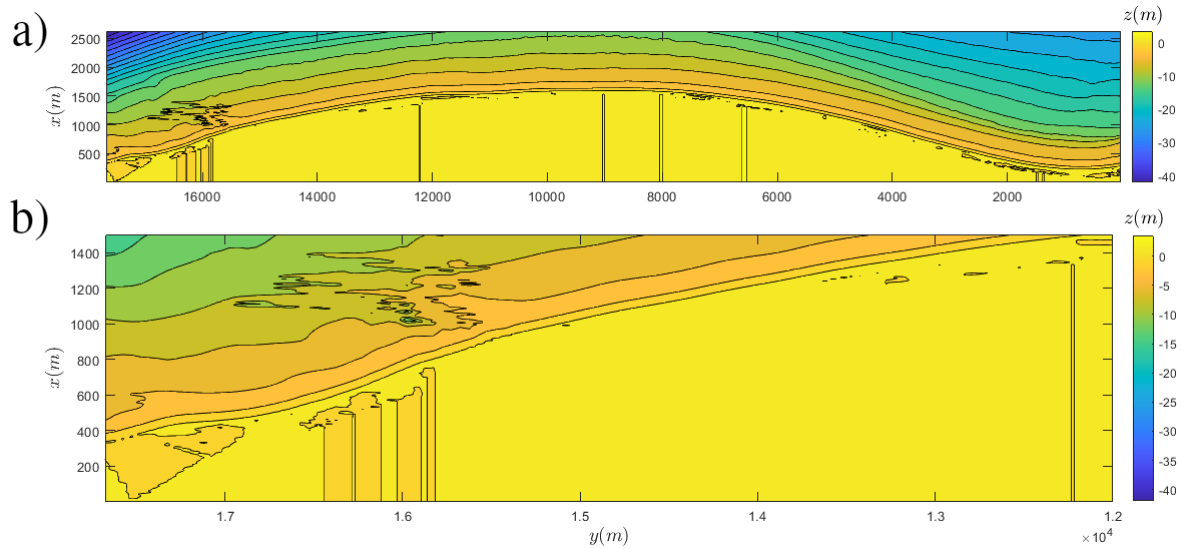

Figure 4.1.1: (a) Example of modelled bathymetry at $t = 775$ d for $f_{eq} = 1$. (b) Zoom of the instability area.

After multiple tests for values within a range of $f_{eq} = \{0.8 \sim 1.3\}$, it was observed that a numerical instability tends to arise in a specific zone of the bathymetry, $17000 > y > 15000$, for values of $f_{eq} \geq 1$ (see figure 4.1.1). The exact origin of this phenomena has not been determined yet, but it is certainly a direct consequence of the feedback relation between the wave climate and the seabed evolution. This claim is supported by the fact that the instability does not appear when the simulations are set with constant wave conditions, instead of the measured wave climate. Since it appears mainly for $f_{eq} > 1$, i.e, for an initial profile below z_{cdf}, it could be related to a recently described instability associated to the cross-shore sediment transport (Falqués *et al.*, 2020). Nonetheless, its emergence is also extremely sensitive to sea level variations and to changes in the parameters that control the morphodynamic evolution.

For values of $f_{eq} < 1$ the instability does not manifest as often and when it does its effects are milder and delayed in time, allowing most of the tests to keep running without blowing up due

to a numerical error. It is also remarkable that, whilst the modelled shorelines for $f_{eq} \geq 1$ present certain tendencies to advance seaward, especially in the central stretch of the coastline, the ones resulting from $f_{eq} < 1$ were more prone to maintaining its initial position. Ultimately, and bearing in mind that not much changes are observed in the actual shoreline for the validation period (section 2.5), the $f_{eq} = 0.8$ is chosen. No lower values than 0.8 are considered in order to not further distort the equilibrium profile from the original Castelldefels beach profile ($z_{be} = f_{eq} z_{cdf}$).

4.2   Validation

The validation has consisted in determining which parameter combinations better adjust to the measured data. First of all, the range of values assigned to each parameter is to be discussed. The parameters to be calibrated are: f_1, f_c, ν, μ, X_{sz}, f_{eq}. The parameter f_{eq} is already fixed to 0.8 in order to avoid the instability. Then, some tests are also conducted for multiple values of $X_{sz} = \{10, 15, 20\}\ m$ (now using the fitted parameter values for ZM and $f_{eq} = 0.8$), and we conclude that its variation has little to no effect on the final modelled results. As a consequence, X_{sz} is settled down to $10\ m$. For each of the remaining parameters, a set of values is assigned in order to proceed with the validation process:

$$f_1 = \{2, 3\}, \quad f_c = \{0.1, 0.15, 0.2\} \tag{4.1}$$

$$\nu = \{0.01, 0.02, 0.03, 0.05\}, \quad \mu = \{0.01, 0.03, 0.05, 0.07\} m^{1/2} s^{-1} \tag{4.2}$$

All of the above intervals are defined using the ZM study as a reference frame. This is assumed to be a reasonable first approach given the similarities shared between both sites and the inherent physical constraints of the calibrated parameters (their value range extent is heavily limited to guarantee numerical stability). For instance, the chosen ν values are those the range used to calibrate in the ZM. In contrast, μ and f_c are restricted to the lower segment of their ZM validation span, that reached values up to $\mu = 0.1\ m^{1/2} s^{-1}$ and $f_c = 0.5$. The reason behind this decision lies in the weak changes observed on the Llobregat delta reference shoreline during the validation period (when compared to the ZM case, see figure 2.5.1). Therefore, values of $\mu > 0.07\ m^{1/2} s^{-1}$ and $f_c > 0.2$ are discarded, limiting both the total along-shore sediment transport and the estimations of D_c (which in turn narrows the morphodynamically active zone). No smaller values for f_c and ν are considered since they are known to lead to the growth of small-scale morphological noise and numerical instabilities (Arriaga, 2017). As for μ, its lower bound is defined following the literature recommendations (Wang & Kraus, 1999). The parameter f_1 defines a minimum value for D_c as a function of D_b and was not used for the ZM. Apart from $f_1 = 2$, a larger value for f_1 has been introduced in this validation, implying in the model a higher lower bound for the instantaneous depth of closure. Each possible combination of the cited parameter values (eqs. 4.1-4.2), a total of 96, is tested with the Q2Dmorfo for the validation period.

The model performance for each possible combination was evaluated with the $RMSSS$ (root mean square skill score) of the modelled contours at $z_b = 0.38\ m$:

$$RMSSS = 1 - \frac{RMSE(Y, X)}{RMSE(B, X)} \tag{4.3}$$

where $RMSE$ stands for the root mean square error, X is a set of n measurements, $x_1, x_2, ..., x_n$, Y is a set of corresponding predictions, $y_1, y_2, ..., y_n$, and B is the prediction of no change (i.e. the initial survey), also known as baseline prediction. The closer to one the $RMSSS$ is, the

more accurate the modelled results are. For the case in hand, X corresponds to the LIDAR yearly reference shoreline, Y to the modelled contour at $z_b = 0.38\,m$ and B to the LIDAR initial reference shoreline of 2012 (notice that, in order to get an accurate $RMSSS$, Y has to be obtained for a time as close as possible to when X was measured). For the RMSSS computation the coastal sections for $y > 17000\,m$ and for $y < 1000\,m$ are excluded in order to avoid the influence of boundary conditions which are rather idealised (see section 3.4). The introduction of this exclusion zone ensures that the validation is not affected by the imposed boundary conditions. There are multiple ways of evaluating the performance of each of the tests through the $RMSSS$. One such way consists on ranking the results suitability based on the mean $RMSSS$ of every available measurement X (4 for the treated case, since LIDAR 2012 is used for the baseline prediction). On the other hand, if the evolution of $RMSSS$ over time stabilises, or if it keeps a marked tendency throughout the validation period, there is no need in computing its mean ($\overline{RMSSS}$), since the last value also serves as an indicator of the modelling performance. After carefully studying the evolution of the simulations' $RMSSS$, it is decided to choose the latter alternative.

Out of the 96 simulations carried out for the validation process, 73 finished successfully, while the remaining 23 ended abruptly before concluding the validation period due to the previously described numerical instability. From the former group, only 33 attained values of $RMSSS$ greater than zero. This means that only these 33 particular parameter combinations achieved better predictions than the baseline prediction or prediction of no change ($RMSSS = 0$).
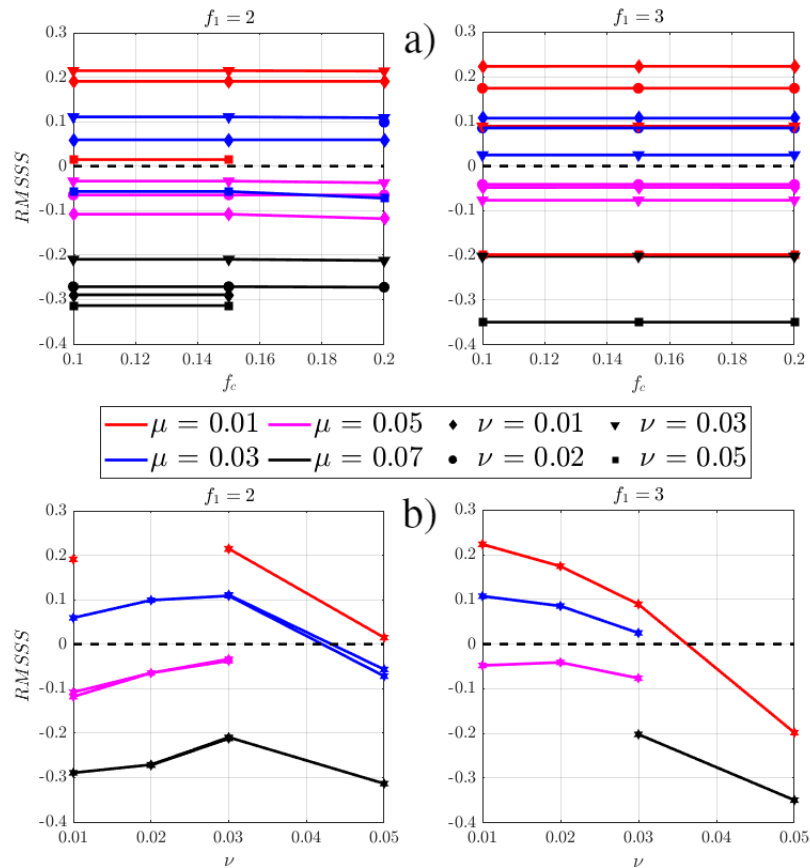

Figure 4.2.1: $RMSSS$ of the $z_b = 0.38\,m$ bathymetric line after almost 5 years, for all the possible combinations of the values assigned to f_1, f_c, ν and μ (from different perspectives: (a) as a function of f_c and (b) as a function of ν)

In figure 4.2.1, all the tests that reached to $t = 1825$ d $= 5$ yr are represented. One can appreciate that the $RMSSS$ values obtained are modest, with only 18 simulations surpassing the 0.1 mark, and just 6 cases above 0.2. This kind of outcome was expected, due to the small variability of the actual shorelines during the validation period (2012-2017). Any deviation of the modelled shoreline with respect to the actual one can amplify irreversibly the $RMSE(Y, X)$ to $RMSE(B, X)$ (difference between the initial and the current reference shorelines) ratio. In summary, low values of $RMSE(B, X)$ (as in our case), lead to small $RMSSS$ (equation 4.3). otice that in figure 4.2.1b only parameter combinations regarding μ, ν and f_1 are discernible, as the different $RMSSS$ obtained when only varying the value of f_c are almost identical, as it can be seen in figure 4.2.1a. Ergo, the effect of changing f_c is virtually imperceptible on the final results. From the mentioned graphs, it is also reasonable to conclude that lower values of μ and ν are to be preferred, with $\mu = 0.01\ m^{1/2}s^{-1}$ and $\nu = \{0.01, 0.03\}$ (for $f_1 = \{3, 2\}$, respectively) since their corresponding simulations achieve higher values of $RMSSS$. The values of $\mu = \{0.05, 0.07\}\ m^{1/2}s^{-1}$ can be directly rejected, as none of the corresponding combinations reaches $RMSSS > 0$. This is a logical result: since the actual shoreline hardly change, the best model parameters are those providing the smallest change.

Even though most of the runs have completed the validation period, there is no way of guaranteeing that the instability will not appear later on when performing the long-term simulations. So rather than choosing a single combination of parameters, multiple combinations are considered in order to have at our disposal a manifold of parameter sets in case that any of the long-term tests fails.

Only the validation simulations with $RMSSS > 0.1$ are considered. Among the cases with $f_1 = 3$, nine in total, and $RMSSS > 0.1$ only those with $f_c = 0.15$ are included. Despite that the results obtained when changing f_c are also really similar this reasoning is not maintained for simulations with $f_1 = 2$. We have decided to prioritise and give more weight to this latter group for being more realistic. Ultimately, 12 combinations of parameter values are selected for the long-term simulations (9 with $f_1 = 2$ and 3 with $f_1 = 3$, see Table 1). The number associated to each test simply refers to the order in which they were performed, and has nothing to do with their performance expectations in the long run.

	f_1	f_c	ν	$\mu\ [m^{1/2}s^{-1}]$	$RMSSS$	$\overline{RMSSS}$
Test 1	2	0.1	0.01	0.01	0.19	0.29
Test 2	2	0.1	0.03	0.01	0.21	0.25
Test 3	2	0.1	0.03	0.03	0.11	0.19
Test 4	2	0.15	0.01	0.01	0.19	0.29
Test 5	2	0.15	0.03	0.01	0.21	0.25
Test 6	2	0.15	0.03	0.03	0.11	0.19
Test 7	2	0.2	0.01	0.01	0.19	0.29
Test 8	2	0.2	0.03	0.01	0.21	0.25
Test 9	2	0.2	0.03	0.03	0.11	0.19
Test 10	3	0.15	0.01	0.01	0.22	0.26
Test 11	3	0.15	0.01	0.03	0.11	0.21
Test 12	3	0.15	0.02	0.01	0.17	0.16

Table 1: Combinations of parameter values chosen to perform the long-term simulations.

e**f**

5 Results of the long-term evolution and discussion

In this section, the results of the long-term simulations are described and discussed. Prior to this, the construction of the time projections for the sea level and wave conditions is explained.

5.1 Wave climate and sea level projections

Before being able to run the long-term simulations with the validated combinations of parameters, it is first necessary to create the data for the Q2Dmorfo. That includes the sea level evolution (with the different sea level rise scenarios) and the wave climate. Since the aim of this project is to obtain predictions up to 2100, and the measured data is available until 2017 there is a 83-years gap of hourly data to be covered.

Contrary to popular belief, there is no scientific evidence that endorses a substantial change in wave climate in the next years or decades, at least not in the Mediterranean sea. If anything, the effects of erosion and sea level rise are going to change the nearshore bathymetry, which in turn will affect the position of the wave-breaking depth, but not the other way around. This project will work under the assumption that no significant changes related to the wave climate will happen in the Llobregat delta during the remainder of this century. In consequence, the wave climate data fed to the model simply consists of a repetition of the measurements used during the validation tests until 2100 (i.e. about 18 iterations of a 5 years long hourly wave series).

Obtaining the future sea level evolution is more complex. The premise however, is similar: we repeat a 5 year sea level baseline to which the corresponding sea level rise projection is added. The sea level baseline is a detrended version of the sea level measurements used during the validation period. The first step is to subtract a linear regression of the measured data to the data itself, in order to eliminate any kind of tendency inherent to the sea level evolution. The outcome is a sea level variation around the NMMA zero (black line in figure 5.1.1). In order to adapt it to the studied site, the measured MSL is added, attaining the desired detrended sea level evolution that oscillates around $z_s = 0.15\ m$ (green line in figure 5.1.1).
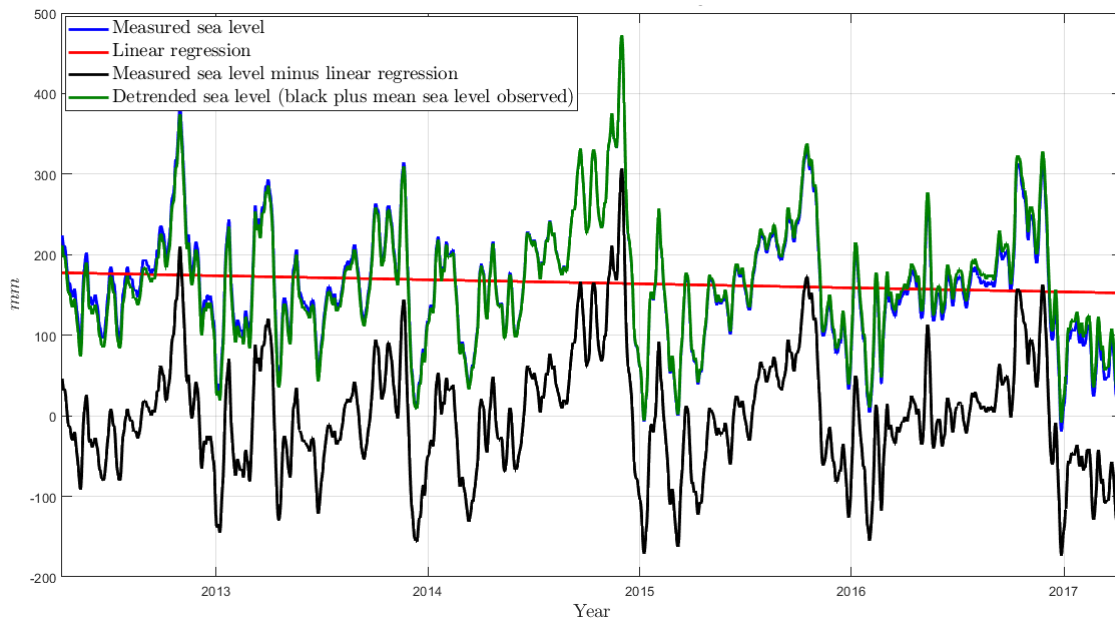

Figure 5.1.1: Detrending process for the sea level measured during the validation period

It is important to proceed in this manner so the estimated projections do not add on to a potential climate change effect already accounted for by the measured data, if there is any appreciable. In fact, a subtle decreasing sea level tendency is found during the validation period (figure 5.1.1) because in temporal scales ~ 10 years the inter-annual fluctuations prevail over the long-term variations, as assessed in Sayol & Marcos (2018). In the end, the computed sea level baseline is similar to the original data (figure 5.1.1).

For this project 6 different scenarios regarding mean sea level rise are examined. Apart from the mean projections for RCP2.6, RCP4.5 and RCP8.5 (described in section 2.3), the most extreme prediction for RCP8.5 is also included, consisting on its mean plus σ the standard deviation of the estimate, and being called RCP8.5+σ. Two other scenarios are used in order to compare the aforementioned cases with the site evolution if there was no sea level rise. One of them consists on repeating the unaltered baseline until reaching 2100 (No SLR), whilst the other simply imposes $z_s = $ MSL throughout the whole simulation. Since the evolution of all the considered scenarios is smooth, a single prediction for each decade is used and a linear regression for the hours in-between is done (figure 5.1.2a). In figure 5.1.2b the final sea level curves are shown, including the concatenated baseline, the chosen MSLR projections and the effect of subsidence. Notice that for the cases where no sea level rise is accounted for, subsidence is also not considered because the objective of such simulations is knowing what happens when neglecting all these long-term effects. It is worth noticing that for the cases that consider sea level rise, no significant differences can be appreciated until 2050 (figure 5.1.2b). Despite these initial similarities, by the year 2100 the mean sea level rise predictions range from 750 mm to over 1200 mm.
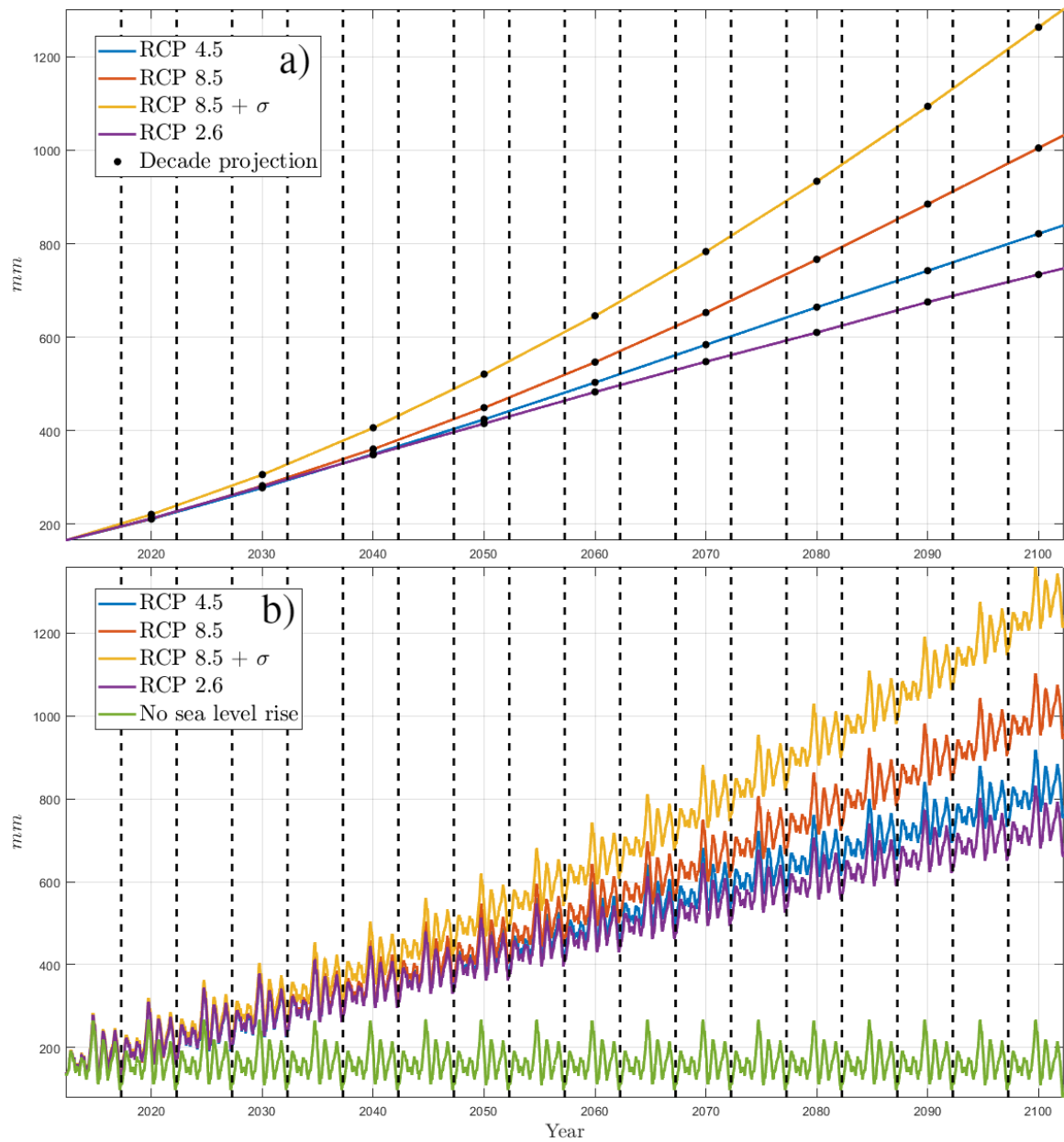
ef

Figure 5.1.2: (a) MSL rise projections with a delta subsidence of 1.5 mm per year. (b) Final sea
level time evolution (dashed lines indicate the end of the 5 year period in the baseline).

5.2   Default case results

5.2.1   Selection of the default case

The first step to describe the results of the long-term simulations is to choose an appropriate default case, among the 12 different combinations of parameter values (table 1). Out of the 76 simulations initially launched (12 tests and 6 sea level scenarios) just one has run up to 2100 ($\sim$ 32800 days). All the others have eventually crushed due to the instability described in chapter 4. Still, from those that prevailed for longer times some conclusions may be extracted. First of all, it is important to distinguish between those simulations carrying valuable information and those that due to their poor performance can already be discarded. In particular, any simulation that does not reach 35 years ($\sim$12775 days) is rejected, because the differences between sea level rise scenarios do not become significant before this temporal mark. Table 2 displays the duration of every simulation:

	RCP2.6	RCP4.5	RCP8.5	RCP8.5+σ	No SLR	$z_s = $ MSL	t_p
Test 1	28650 d	27500 d	26300 d	2600 d	14050 d	4950 d	50 d
Test 1	28600 d	27400 d	26200 d	2600 d	14000 d	4800 d	100 d
Test 1	8000 d	24400 d	22400 d	18200 d	4200 d	600 d	200 d
Test 2	9400 d	22200 d	6000 d	6200 d	20000 d	23200 d	200 d
Test 3	12000 d	8600 d	9400 d	4800 d	2200 d	200 d	200 d
Test 4	8000 d	23000 d	22400 d	18200 d	4000 d	600 d	200 d
Test 5	600 d	9400 d	22400 d	6000 d	20000 d	22800 d	200 d
Test 6	11800 d	8600 d	9400 d	4800 d	2200 d	400 d	200 d
Test 7	2600 d	10000 d	800 d	400 d	29200 d	10400 d	200 d
Test 8	10600 d	19400 d	9800 d	2200 d	15600 d	13400 d	200 d
Test 9	11800 d	12000 d	1000 d	600 d	6000 d	6200 d	200 d
Test 10	200 d	3600 d	8000 d	18200 d	2600 d	30400 d	200 d
Test 11	6600 d	2600 d	11800 d	7600 d	12200 d	12800 d	200 d
Test 12	32800 d	600 d	1000 d	2600 d	1200 d	4600 d	200 d

Table 2: Duration in days of each of the long-term simulations performed. In green simulations that have lasted for 35 years (12775 days) or longer; in red, those that do not reach the end of the 5 year long (1825 d) validation period. With t_p being a parameter that determines the frequency of outputs in Q2Dmorfo.

In terms of the duration of each of the parameter combinations, the poor performances of tests for $\mu = 0.03\ m^{1/2}s^{-1}$ are to be highlighted. Just one of the simulations out of the four tests with this μ value (Test 3, Test 6, Test 9 and Test 11) has been able to model beyond 35 years, whereas others crushed even before arriving to the end of the validation period. Also, the simulations that use $f_1 = 3$ were less satisfactory than their counterpart $f_1 = 2$, with the exception of Test 12 RCP2.6, that has been the only case to achieve predictions for the desired lapse of time ($\sim$ 90 years). For other parameters, i.e ν and f_c, it is difficult to form a criteria just out of their temporal duration. However, some remarks may be opportune. For instance, the tests that seem to behave better, and last for longer, in the SLR cases are those with $\mu = 0.01\ m^{1/2}s^{-1}$ and $\nu = 0.01$, whilst those with $\mu = 0.01\ m^{1/2}s^{-1}$ and $\nu = 0.03$ appear to prolong the scenarios where SLR is not accounted for. Regarding to f_c, little difference can be found between Tests 1 & 4 ($f_c = \{0.1, 0.15\}$, respectively) and between Tests 2 & 5 ($f_c = \{0.1, 0.15\}$, in that order), as far

as modelling simulation time is concerned. However, Tests 7 & 8 ($f_c = 0.2$) display a completely different behaviour. Tests 3, 6 & 9 ($f_c = \{0.1, 0.15\}$) do also evolve similarly, probably due to the influence of $\mu = 0.03\ m^{1/2}s^{-1}$.

One may wonder how it is possible that the same simulations that completed the validation process are now unable to model the same lapse of time (cells marked in red). The reason behind this behaviour lies in the changes introduced in sea level. Analysing table 2 it can be appreciated how sensitive the triggering of the instability is to sea level variations. For example at $t = 600$ d the sea levels for scenarios RCP2.6 and RCP4.5 are almost identical. Nonetheless, for Test 5 the first simulation ends abruptly at this time whilst the latter continues until $t = 9400$ d. It is important to bear in mind that for different simulations of a same test only the sea level projections change, therefore, these must play a relevant role in the instability development. Another case that may cause confusion, is the no SLR scenario for Test 12, which does not reach the end of the validation period either. Despite not considering sea level rise in this scenario, recall that a minor detrending of the sea level has been introduced, which may explain why now this simulation triggers the appearance of the instability sooner.

Test 1 is chosen as the default case ($\mu = 0.01\ m^{1/2}s^{-1}$, $\nu = 0.01$, $f_c = 0.1$ and $f_1 = 2$) because it is the test that objectively achieves a better performance for the SLR scenarios out of the 12 initially considered (Table 2, lines 3 to 14). In order to obtain a clearer insight on the origin of the instability, some extra simulations have been launched for this test. These consisted in using lower values of the parameter t_p (Table 2, lines 1 and 2), a constant that determines the frequency of outputs in Q2Dmorfo. For every $t_{out} = k \cdot t_p$ with $k \in \mathbb{N}$, a group of variables such as z_b or x_s are updated to be written in output files. This parameter was not included in the validation process since, in principle, it is not supposed to affect the final modelled results. Nevertheless, it turns out that the results obtained for $t_p = \{50, 100\}$ d differ from those achieved with $t_p = 200$ d, due to the small numerical differences that arise due to the update of z_b and x_s.

Under the assumption that, within the simulations that avoid the instability triggering, results should be independent of t_p, the final simulations of Test 1 are chosen to be the better performing simulations for each scenario, independently of the assigned value of t_p (table 3). Hence:

	RCP2.6	RCP4.5	RCP8.5	RCP8.5+σ	No SLR	$z_s = \text{MSL}$
Test 1	28650 d	27500 d	26300 d	18200 d	14050 d	4950 d

Table 3: Duration of the final simulations used fot Test 1 for every scenario considered.

5.2.2 Characterisation of the default case results

As justified in the previous section, Test 1 is used as default simulation. The scenario RCP8.5 is chosen as the default one for being the most probable according to the experts. After carefully examining the results of Test 1, some general patterns in the Llobregat delta long-term evolution can be recognized. This also allows to characterise its development independently of the parameters used in each simulation because all tests agree in most aspects of the morphodynamic evolution of the site(which is an indication of the Q2Dmorfo consistency). Without addressing the exclusion zone ($y < 1000\ m$ and $y > 17000\ m$), three regions with markedly distinct evolution behaviour are differentiated: the northern zone ($15000 < y < 17000\ m$), the central zone ($9500 < y < 15000\ m$)and the southern zone ($1000 < y < 9500\ m$), as depicted in figure 5.2.1.
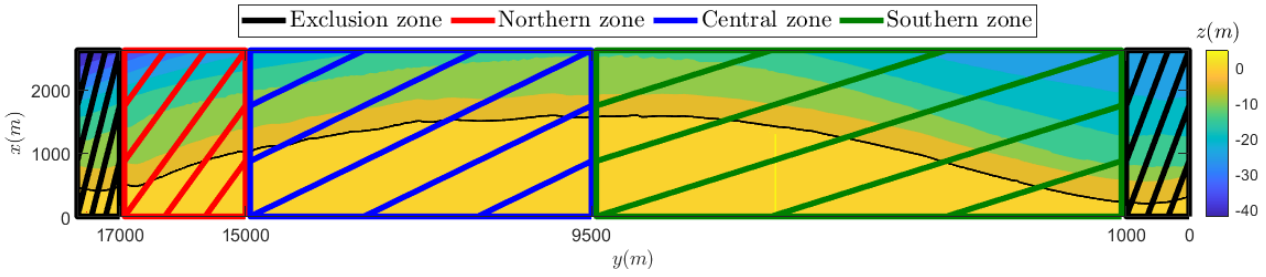
Figure 5.2.1: Proposed divisions for the Llobregat delta according to their modelled morphodynamic behaviour.

The northern zone, the closest to the Llobregat mouth, is where the regression of the modelled shoreline is more ostensible, and in consequence, the region where there is more loss of dry beach area. In figure 5.2.2 it can be perceived how a substantial part of the modelled shoreline of the northern zone already lies behind the LIDAR landward limit (back-end of the dry beach). This is probably one of the most relevant results obtained throughout this project: if the estimates are correct, for the most likely climate change scenario (RCP8.5) some parts of El Prat del Llobregat may be already left with no dry beach or even under flooding risk before reaching the year 2080, if there is not a proper coastal management.
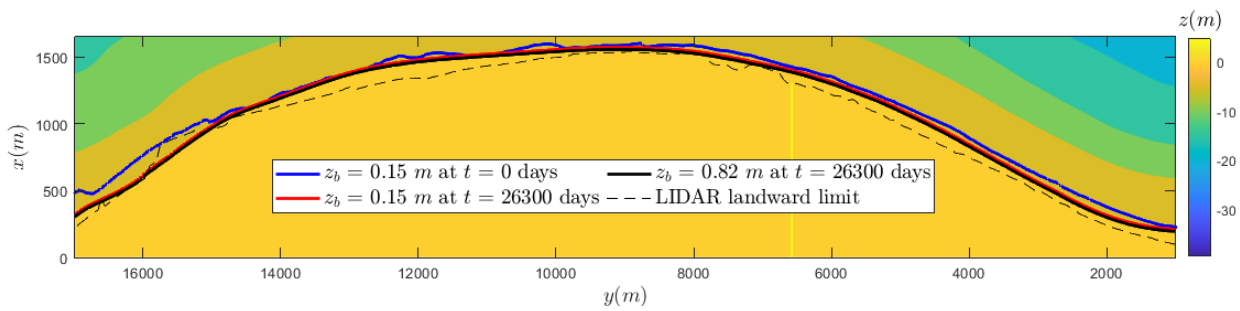
Figure 5.2.2: The shoreline obtained for Test 1 scenario RCP8.5 at $t = 26300$ days (year $\sim$2080) (black line), the depth contour at $z_b = 0.15\ m$ (red line), the initial shoreline (blue line) and the LIDAR landward limit (black dashed line) are represented. Notice that the x-axis has been exaggerated to better discern the represented coastlines.

Figure 5.2.3 displays the differences between initial and final shorelines to better visualize the changes. The alongshore average shoreline recession is also shown in figure 5.2.4b. Another important quantity that has been computed is the total horizontal area, from the shoreline to the back-end of the dry beach. In Test 1 scenario RCP8.5 at $t = 26300$ days an area loss of over 113 % was recorded (notice that the actual dry beach area is comprised between the landward limit of the LIDAR and the current shoreline) with a mean beach retreat of 120 m (figure 5.2.4 red lines). It is interesting to remark that most of the shoreline recession that experiences the northern zone comes from morphodynamic erosion rather than from pure sea level rise inundation. To have an estimate on which percentage of the recession corresponds to the effect of erosion, one can compute the differences between the initial shoreline at $z_b = \mathrm{MSL}(t = 0) = 0.15\ m$ and the modelled isobathymetric contour at the same height for a time t, and then reckon to what portion of the total coastline recession it accounts for (see figure 5.2.3). For the northern zone in 2080 a 85-15 % relation between erosion and inundation has been identified, the highest in all the domain (figure 5.2.3).
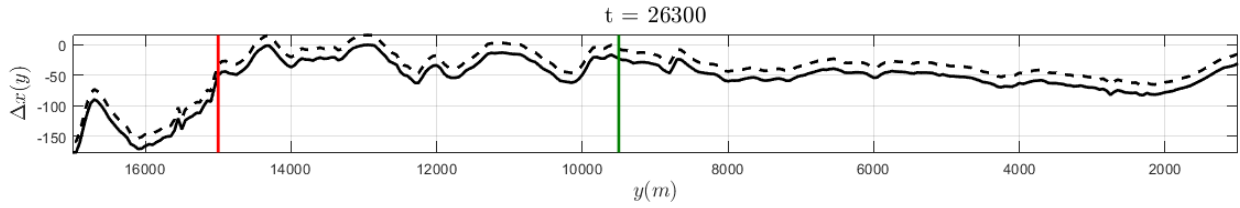
Figure 5.2.3: Difference between the cross-shore positions of the initial shoreline and the modelled shoreline in 2080 for Test 1 scenario RCP8.5 (continuous line). The dashed line represents the pure morphological erosion, i.e., the difference between the original shoreline and the contour $z_b = 0.15\ m$.

The central zone shows a very different behaviour with respect to the one presented for the northern zone. Most of the shoreline experiences little retreat, without changing its initial position on average, even for those scenarios that contemplate extreme sea level rise (figures 5.2.3 and 5.2.2). It is clearly the most resilient region to area loss (figure 5.2.4). For Test1 scenario RCP8.5 at $t = 26300$ days, the dry beach area of this zone is reduced in a 25% and a mean shoreline recession of around 30 m is registered. The erosion to inundation percentages until 2080 turn over to be a 40-60% so, unlike the northern zone, most of the perceived retreat is caused by pure SLR inundation. Interestingly enough, some positions within this region even display a morphodynamic tendency to accretion, however, the opposed inundation process provoked by SLR ends up overcoming this tendency.

The southern zone, within which Castelldefels and Port Ginesta are located, also undergoes a regressive evolution, but its mean shore retreat is not as pronounced as in the northern zone (figures 5.2.3 and 5.2.2). Both of its delimiting borders maintain a quite invariant position. For Test1 scenario RCP8.5 at $t = 26300$ days, an area loss corresponding to the 46% of the initial dry beach area is observed, accompanied by a mean recession of the shoreline close to 50 m (figure 5.2.4). Since it is the largest region, its area loss rate and its departure from the initial shoreline resemble the mean evolution of the site as a whole. The same happens for its erosion to inundation percentages: 70-30% in 2080.
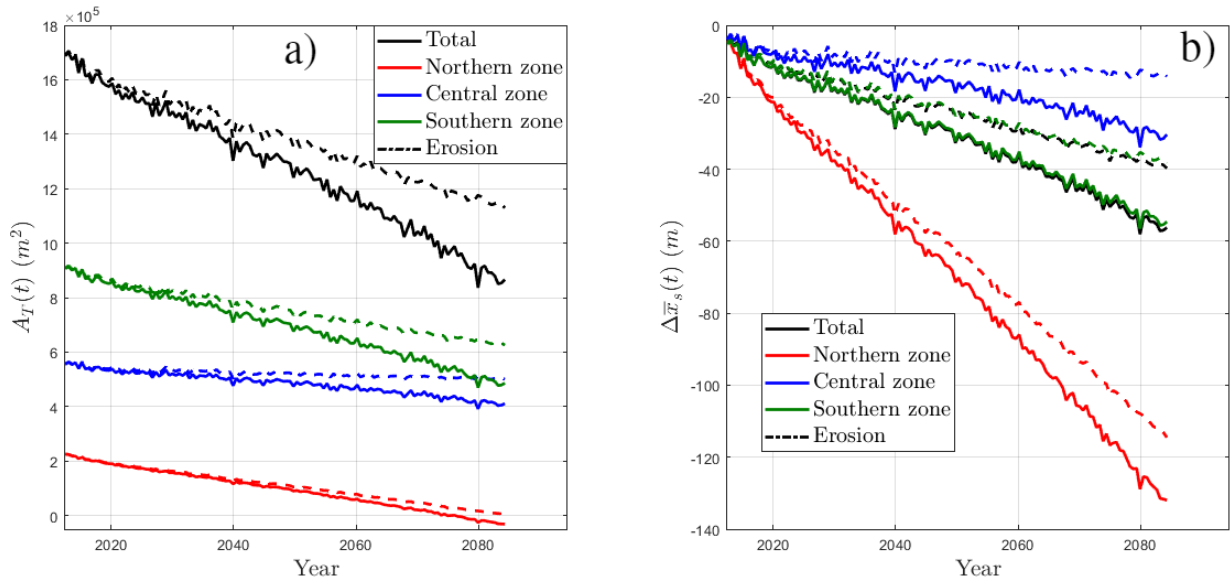

Figure 5.2.4: (a) Total dry beach area evolution over time for each of the site zones, and (b) evolution of the modelled shoreline mean departure from the initial shoreline for Test 1 and scenario RCP8.5.

On a global perspective, the delta as a whole is receding, but that each of its regions does so at different speeds. Its form is also evolving into a more gaussian-shaped outline. In terms of total area evolution, Test 1 scenario RCP8.5 estimates that almost half of all the initial dry beach area will be gone by 2080, with a mean departure from the 2012 shoreline of about 50 m landward (see figure 5.2.4). The global erosion-inundation relation found for all mean sea level rise scenarios (RCP2.6, RCP4.5 and RCP8.5) oscillates around 70-30% by 2080.

In figure 5.2.5 the differences between the initial and final ($t = 26300$ days) are portrayed. From there it is possible to observe how the deep bathymetry remains almost unchanged, as expected. This contrasts with the region immediately before the Llobregat's mouth, that has become considerably deeper. This may be indicative of a strong alongshore flux that transports sediment from there towards the central region, since it is the only area that displays some signs of accretive evolution. Nonetheless, it is hard to be certain if such accumulative behaviour does actually exist, as it gets distorted by the computed SLR. One way of obtaining a clearer perception of this matter is to analyse a simulation where no SLR is taken into account.
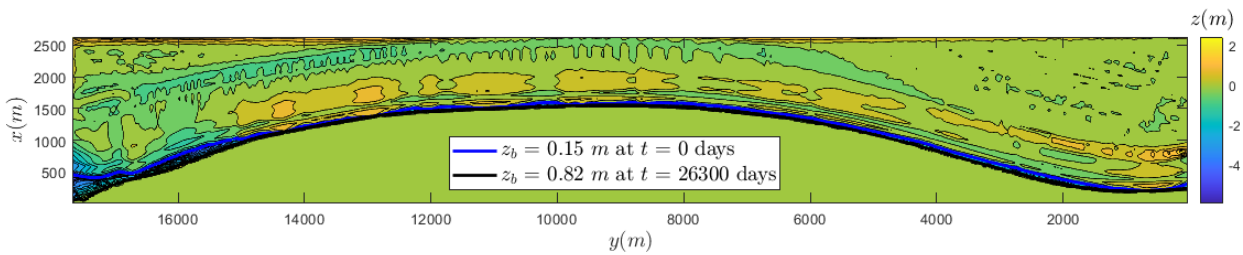
Figure 5.2.5: Bathymetric changes ($\Delta z(x, y)$) between the initial and final ($t = 26300$ days) bathymetries obtained for Test 1 scenario RCP8.5.

The default No SLR case selected has been that of Test 7 (the one with the best performance for this scenario) because it has exactly the same parameters as Test 1, with the sole exception of f_c. During the validation process, evidence pointed that the value of f_c has little to no impact in the overall results. From figure 5.2.6a one can clearly appreciate that, whilst the southern zone maintains a constant area throughout time, the northern and central zones evolve almost symmetrically in opposite directions. The transformation of these areas occurs in such a way that most of the sand lost in northern zone moves to the central zone, probably due to the alongshore sediment transport. This flux, that does not seem to relent for the modelled time period, provokes a mean beach advance in the central zone of over 10 m by the year 2090, according to the estimates of the simulation. Apart from explaining the accretive nature of the central zone, this simulation also confirms that most of the retreat in the northern zone comes as a consequence of erosion effects. The northern zone coastline retreats a mean value of almost 90 m by 2090, while losing more than half of its original dry beach area (figure 5.2.6). Nonetheless, the total area and mean shoreline of the delta seem to stabilize over time

The fact that such an alongshore transport exists in the area where the instability appears (i.e, $17000 > y > 15000\ m$) gives the impression of being more than a mere coincidence. If the instability and this alongshore transport were related, this would explain why simulations with higher values of μ are unable to model the Llobregat delta without inducing model instabilities.
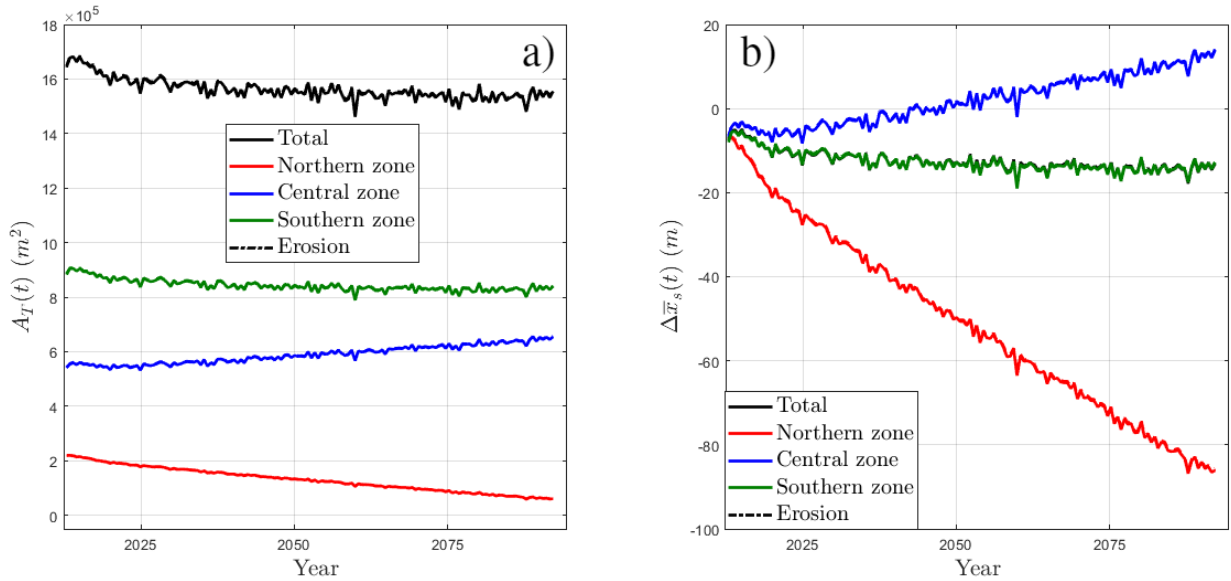
Figure 5.2.6: (a) Total dry beach area evolution over time for each of the site zones, and (b) evolution of the modelled shoreline mean departure from the initial shoreline for Test 7 and scenario No SLR.

5.2.3   Episodes of extreme inundation

In order to assess the impact of MSLR, it is important to quantify the episodes of extreme inundation that can occur due to storm surges that are particularly large and can be specially dangerous if they are superimposed to a high MSL. As mentioned in section 2.3, sea level fluctuations in the Mediterranean are not particularly pronounced. Consequently, the flooding events that may take place in the modelled bathymetry do not change significantly the resulting shoreline.

In order to illustrate this the 99th percentile of the sea level during the validation period, i.e. the sea level that is only overcome 1% of the time during this lapse of 5 years, has been considered. This inundation event would be equivalent to increasing the sea level at a certain time by an extra $0.266\,m$. In figure 5.2.7 the differences between the shorelines corresponding to the MSL and to the extra flooding are represented. Notice that the depicted Δx does not exceed -7 m, even though one of the scenarios that accounts for a greater SLR has been chosen (RCP8.5). The existence of a sand elevation ($1.5 \sim 2$ m) in certain regions prevents the shoreline from approaching LIDAR's landward limit. For the central zone this elevation reaches even higher values (in some cases $\sim$5 m) which would explain why it appears to be more resistant to inundation episodes.
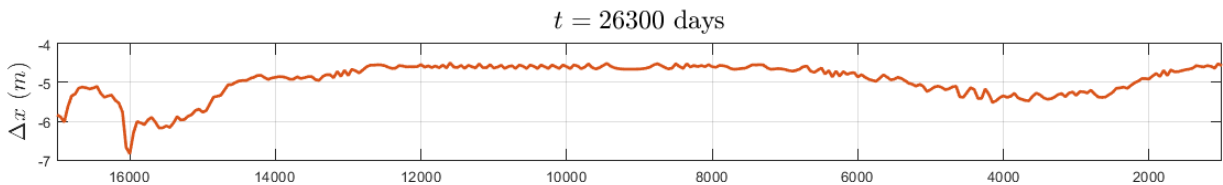

Figure 5.2.7: Difference between the RCP8.5 shoreline corresponding to $z_s = \mathrm{MSL}$ and the one in an inundation event of $z_s = \mathrm{MSL} + 0.266m$ at $t = 26300$ ($t = 18200$) days

5.3   Role of sea level changes

In Test 1, five out of the six proposed scenarios reach beyond 35 years (i.e. RCP2.6, RCP4.5, RCP8.5, RCP8.5+σ and No SLR) and therefore, these 5 scenarios can be compared using Test 1 results. The case of constant sea level, $z_s = 0.15\ m$, is analysed using the results of Test 2, comparing it with those of the scenarios RCP4.5 and No SLR of that test. As Test 1 and Test 2 only differ in the value of the parameter ν, some parallelisms can be established between both comparisons. Figure 5.3.1 shows all the scenarios of Test 1 that consider MSLR and the one that does not. Both the total area and the mean deviations from the initial shoreline tend to stabilise over time for the No SLR simulation. By contrast, in the other projections these measures decrease in an almost linear way (specially in the long-term). As it was to be expected, the projections that account for a greater increment of the MSLR also involve a larger loss of total area and a more pronounced retreat of the shoreline. Table 4 shows the percentage of loss of dry beach area (with respect to the initial bathymetry) for each scenario, at two different moments (2050 and 2075).

	RCP2.6	RCP4.5	RCP8.5	RCP8.5+σ	No SLR
2050	21.37 %	24.76 %	26.14 %	27.89 %	6.50 %
2075	36.53 %	37.91 %	43.01 %	-	-

Table 4: Percentage of lost area for different scenarios of Test 1

It is also interesting to see that the contribution of the morphological erosion (computed using the isobathymetric $z_b = 0.15\ m$ instead of the actual shoreline) to the total evolution seems to decay progressively throughout time. Notice that this decay is even more marked for RCP8.5+σ. It is also noticeable how long it takes for significant differences to appear for the distinct SLR projections. For instance, RCP4.5, RCP2.6 and RCP8.5 effects on area and shoreline evolution are similar until year 2050, but they differ after this time mark is reached. This can also be seen in figure 5.3.2, where for the year 2050 shoreline changes corresponding to RCP2.6, RCP4.5 and RCP8.5 are almost identical, whereas by 2085 some differences can be perceived, specially in the case of RCP8.5.
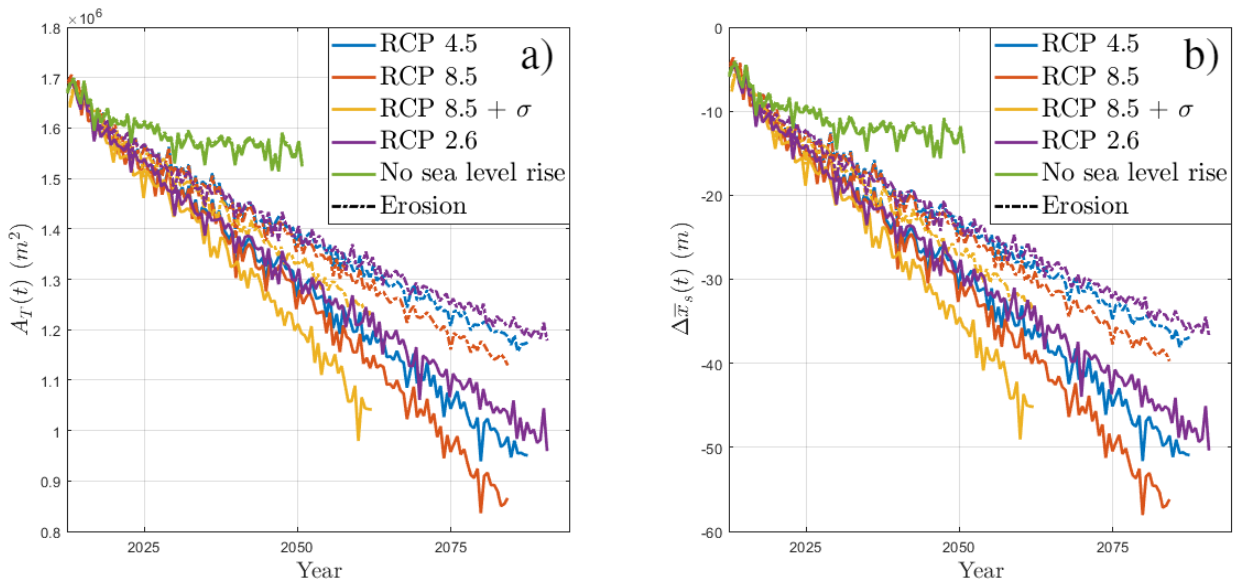

Figure 5.3.1: (a) Total dry beach area evolution over time, and (b) evolution of the modelled shoreline mean departure from the initial shoreline for different MSLR scenarios of Test 1.
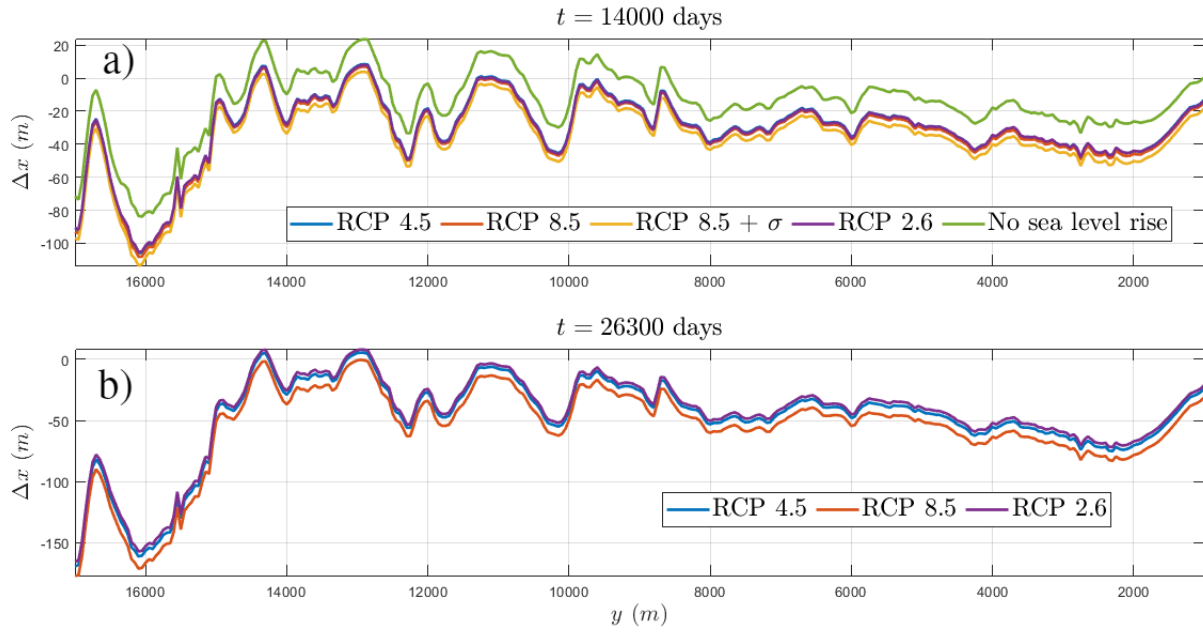
Figure 5.3.2: Shoreline changes (Δx) for different MSLR scenarios of Test 1 in (a) 2050 and (b) 2085.

Figures 5.3.3 and 5.3.4 show the simulation results of Test 2 for both NSLR scenarios and that of RCP4.5 for the sake of comparison. The first noticeable thing about the $z_s = 0.15\ m$ simulation is that, even though it presents similarities with the No SLR projection, its regressive effect over the delta is much smaller. This can be easily perceived by observing the figure 5.3.3b, where the mean shoreline departure for No SLR oscillates around 18 m, reaching 25 m in some occasions, whilst for the $z_s = 0.15\ m$ it never surpasses retreat values of 14 m. Which may not seem much at first, but one has to consider that the only difference between both simulations is the introduction of the sea level variability in the No SLR scenario. Therefore, any erosive process of the No SLR simulation that does not take place in $z_s = 0.15\ m$, can be directly accounted to the effect of sea level fluctuations, which contributes to a loss of 1% of the total area by 2050. Another distinctive and logical characteristic is the smoothness with which the $z_s = 0.15\ m$ tends to stabilization, when compared to the other considered scenarios (including the No SLR). Overall, simulation with $z_s = 0.15\ m$ results does not give much information about the natural evolution of the delta, since its premise of a constant MSL is unrealistic, so from now on it is not further described.
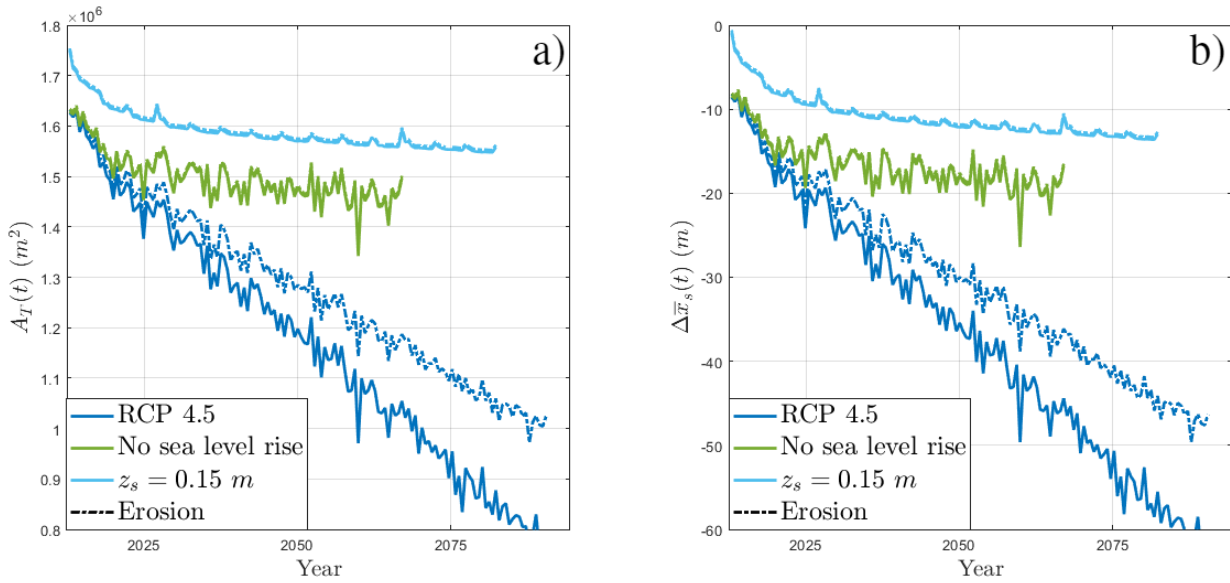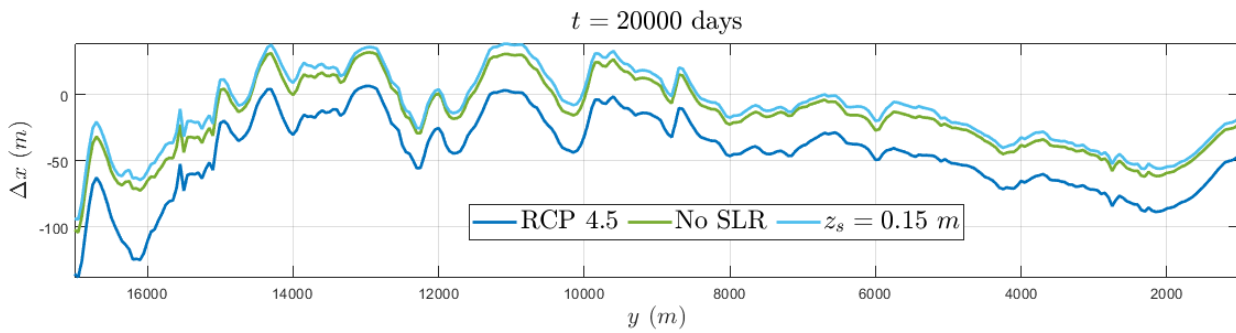
Figure 5.3.3: (a) Total dry beach area evolution over time, and (b) evolution of the modelled shoreline mean departure from the initial shoreline for different MSLR scenarios of Test 2.

Figure 5.3.4: Shoreline changes (Δx) for different MSLR scenarios of Test 1 in 2065.

5.4 Role of model parameters

To analyse the effect that varying each of the calibrated parameters (i.e. f_1, f_c, ν and μ) has in the long-term evolution, a group of two or more simulations that only differ in the parameter under study are selected in each of the cases. When the conditions allow it, two comparisons are performed: one for the SLR projections and another for the NSLR ones. Simulations that do not reach beyond 35 years (~ 12775 d) are only used if there is no alternative.

5.4.1 Effect of f_1

There are only two tests whose parameters differ only for f_1 and those are Tests 4 (with $f_1 = 2$) and 10 (with $f_1 = 3$). As the only projection that reaches over 35 years for both tests is RCP8.5+σ, this is the one that we compare. In figure 5.4.1 one can see that, even though both cases evolve in a similar manner, the simulation with $f_1 = 3$ accounts for a greater loss of area and a larger retreat of the shoreline. More specifically, by year 2060, Test 10 simulation has lost a 9% more of the initial area and retreated $10\,m$ more than the Test 4 case. Most of the additional area lost for $f_1 = 3$ proceeds from the southern zone, whilst the evolution of the northern and central regions remain as in simulations with $f_1 = 2$.

The parameter f_1 determines at which depth the Q2Dmorfo searches for the breaking depth (D_b). When increasing the value of f_1 a more regressive behaviour is observed because the model is actually able to find greater D_b, which in turn broadens the surf zone, where most of the sediment transport occurs.
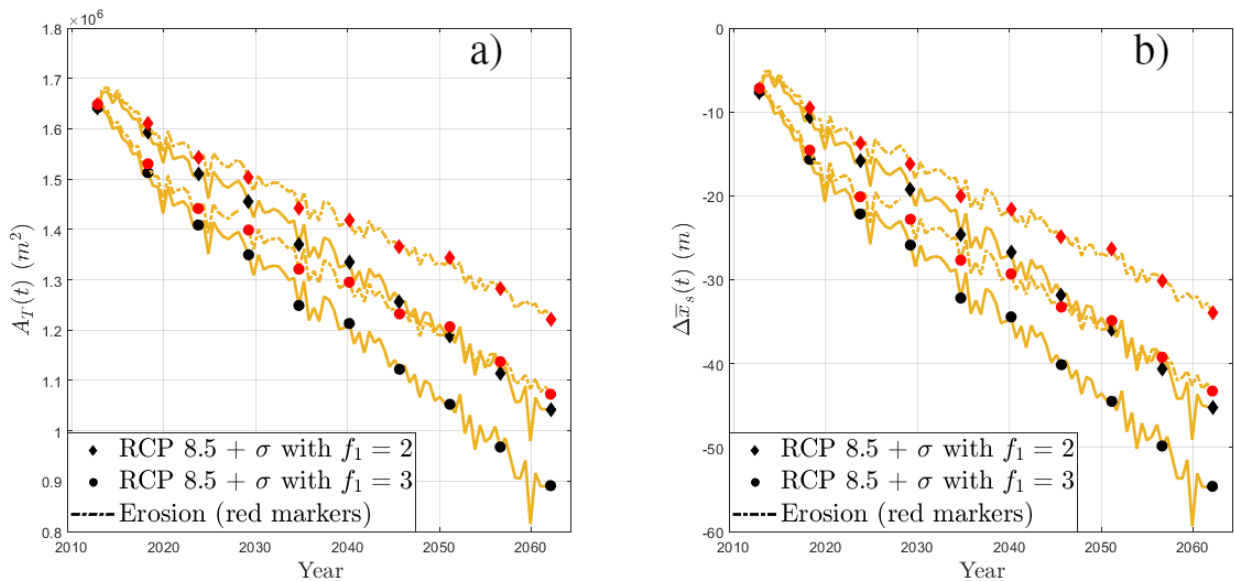

Figure 5.4.1: (a) Total dry beach area evolution over time for RCP8.5+σ's of Tests 4 and 10. (b) Evolution of the modelled shoreline mean departure from the initial shoreline.

5.4.1   Effect of f_c

There are three trios of simulations that only differ in the value of f_c and reach long enough simulation times: Tests 1, 4 & 7 amd Tests 2, 5 & 8 . From these, scenario RCP4.5 of Tests 1 & 4 will serve to understand the impact of the parameter in SLR simulations, whereas the No SLR scenario of Tests 2, 5 & 8 will also be considered since it covers all the contemplated values of f_c. In figure 5.4.2 the evolution of all the aforementioned simulations are represented, however, it is impossible to discern which is which as the results are identical. Some minor differences do exist between $f_c = 0.2$ and $f_c = \{0.1, 0.15\}$, but they are really small. In light of these results, one may conclude that the results are not as sensitive to the change of f_c, and in turn of the depth of closure D_c, as was originally thought.
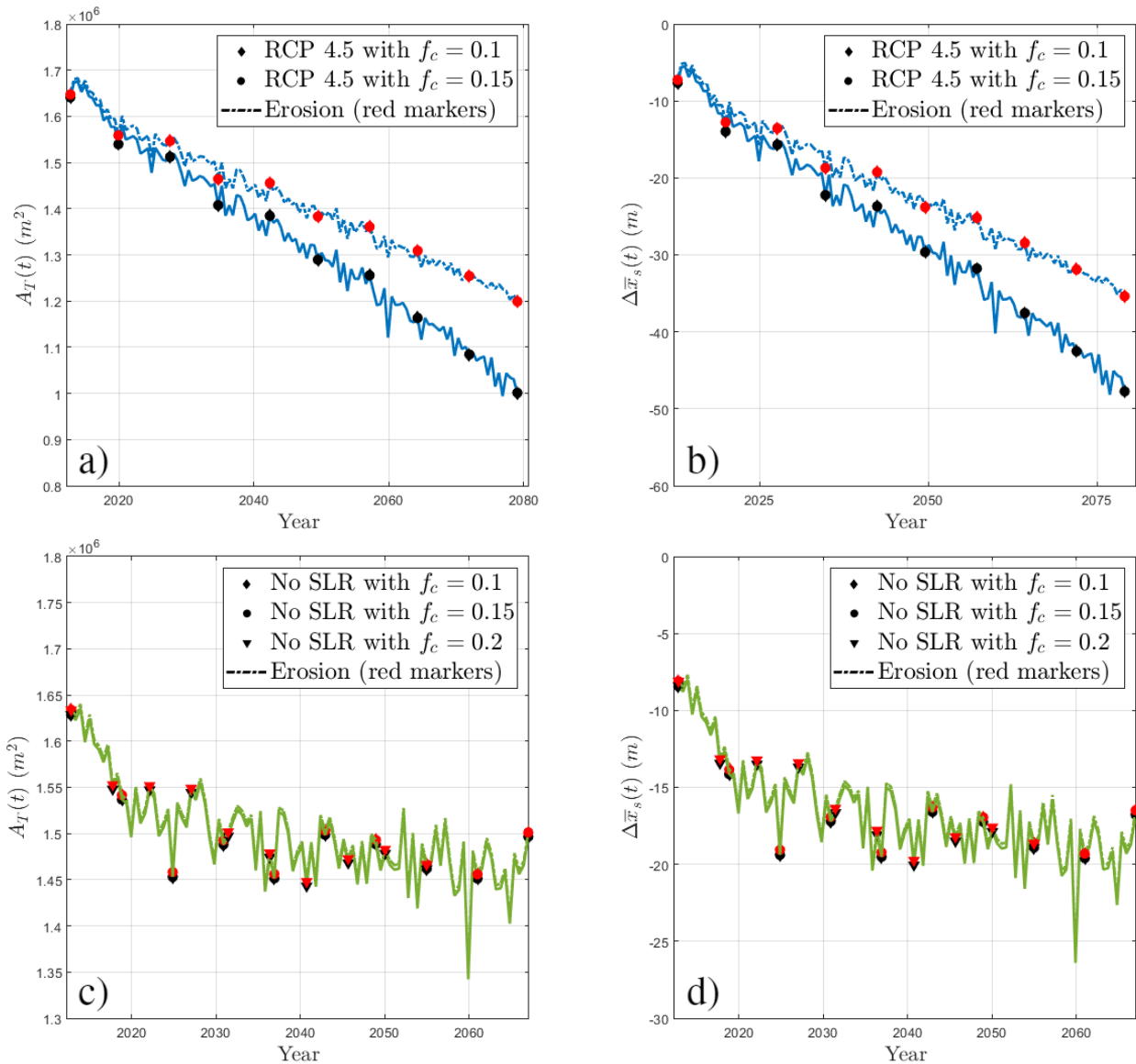
Figure 5.4.2: a) (c)) Total dry beach area evolution over time for RCP4.5 of Tests 1 and 4 (No SLR of Tests 2, 5 and 8). b) & (d)) Evolution of the modelled shoreline mean departure from the initial shoreline.

5.4.1 Effect of ν

To evaluate the impact of ν in the simulations, the scenario RCP4.5 of Tests 1 & 2 is used, as they last long enough. The No SLR scenario of the same tests can be also compared. As it was expected, the simulations with greater values of ν display a more regressive behaviour (see figure 5.4.3). Specifically, scenario RCP4.5 of Test 2 ($\nu = 0.03$) by 2050 registers a 6% more area loss and a mean beach regression 7 m greater than the same projection of Test 1 ($\nu = 0.01$). For the No SLR cases, this differences are reduced to a 4% and 5 m, respectively. As happened for f_1, most of the extra area loss for higher values of ν comes from the southern zone rather than from the northern region. Nonetheless, in this case northern and central areas do also experience more regression for higher values of ν, but this change is not as pronounced as the one that undergoes the southern zone, when compared to the values obtained for $\nu = 0.01$.
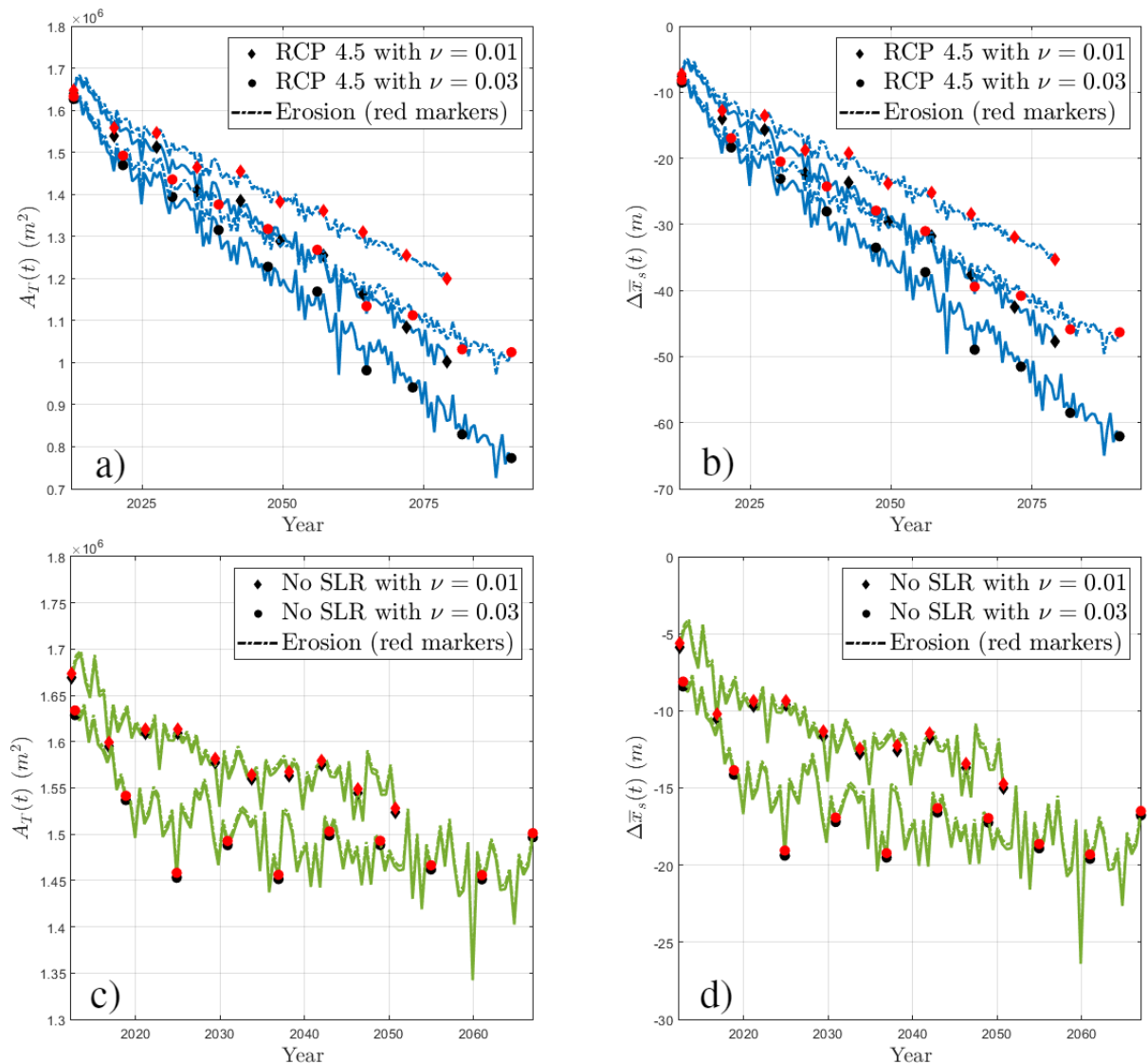

Figure 5.4.3: a) (c)) Total dry beach area evolution over time for RCP4.5 (No SLR) of Tests 1 and 2. b) & (d)) Evolution of the modelled shoreline mean departure.

ef

5.4.1 Effect of μ

The poor performances of simulations with $\mu = 0.03 \; m^{1/2}s^{-1}$ leave only one option available for comparison: the scenario with constant $z_s = 0.15 \; m$ of Tests 10 & 11. Surprisingly, figure 5.4.4 shows that the simulation with $\mu = 0.01 \; m^{1/2}s^{-1}$ gives more erosion than the one with $\mu = 0.03$ $m^{1/2}s^{-1}$. To be more exact, by 2045, the simulation $z_s = 0.15 \; m$ belonging to Test 10 has lost a 3% more area and its shoreline has retreated 3 m more than the Test 11 case. This seems to be counter-intuitive, since what one would expect is that increasing the value of μ the sediment alongshore transport would also raise, and with it the total regression of the site. However, what happens for $\mu = 0.03 \; m^{1/2}s^{-1}$ is that the alongshore transport does in fact grow, but does so in such an effective way that the area lost by the northern shore is immediately recovered by the central zone, so both cancel out, leaving the total dry beach area unchanged. Something similar happens for the southern zone, with the difference that in this case the sediment does not even change of division, so the southern zone area does also remain constant in time.
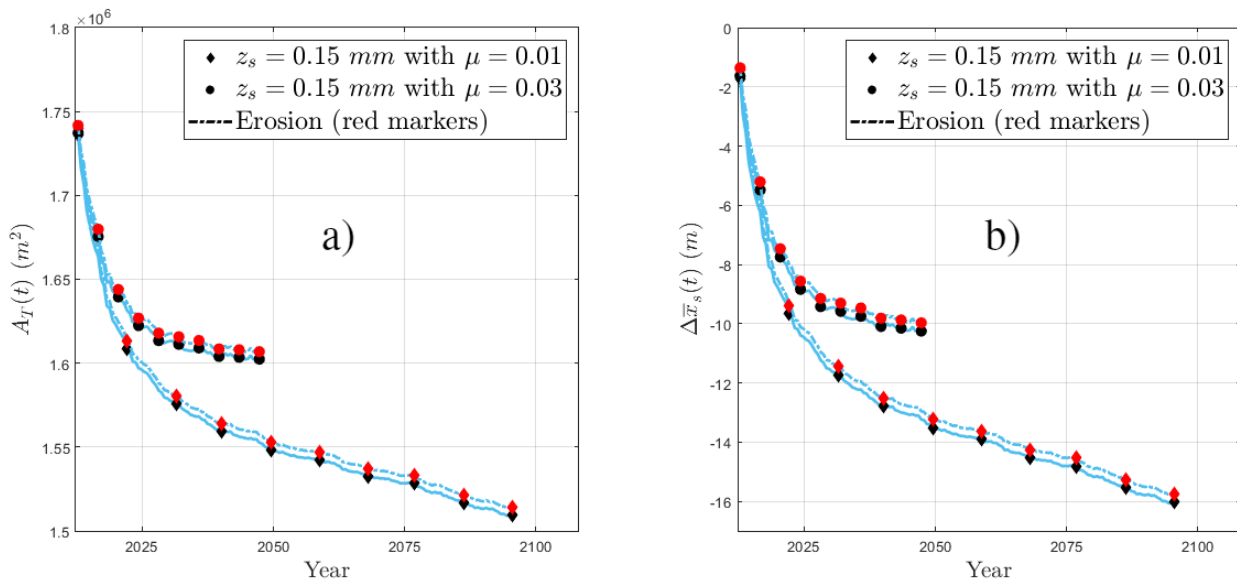

Figure 5.4.4: (a) Total dry beach area evolution over time for $z_s = 0.15 \; m$ of Tests 10 and 11. (b) Evolution of the modelled shoreline mean departure from the initial shoreline.

5.5 Last-minute simulations that skip NaNs

Before concluding this chapter, it is interesting to comment that an attempt to avoid the instability has been made for a set of simulations with the Test 1 parameters. The idea behind it is very simple, maybe even a bit naive. It literally consists in not taking into account those bathymetry updates that may have led to numerical errors. The origin of the instability is first announced by the appearance of NaNs in a very specific region of the delta. Thereby, every time a NaN is detected, the zone in where it is spotted is not actualised for that time step. This arrangement does make sense under the assumption that the instability comes as a result of punctual combinations of the chosen parameters and the data fed to the model, however there is no way of knowing beforehand how many times the model will skip the update of a certain area. The results of these simulations are depicted in figure 5.4.5. From there, one can appreciate that most of the simulations now reach until year 2100, as it was originally intended. The scenarios RCP8.5 and RCP8.5+σ do not last that much, as their bathymetry values eventually became distorted beyond any plausible physical meaning. The other cases however, follow a similar trend

to that of their predecessors. Although the results achieved look promising, further tests would have to be performed in order to guarantee their validity, and this is the main reason why these results have not been used in this project. Nonetheless, we have mentioned them here since they open a path to better understand the triggering of the instability and, in consequence, to deal with it.
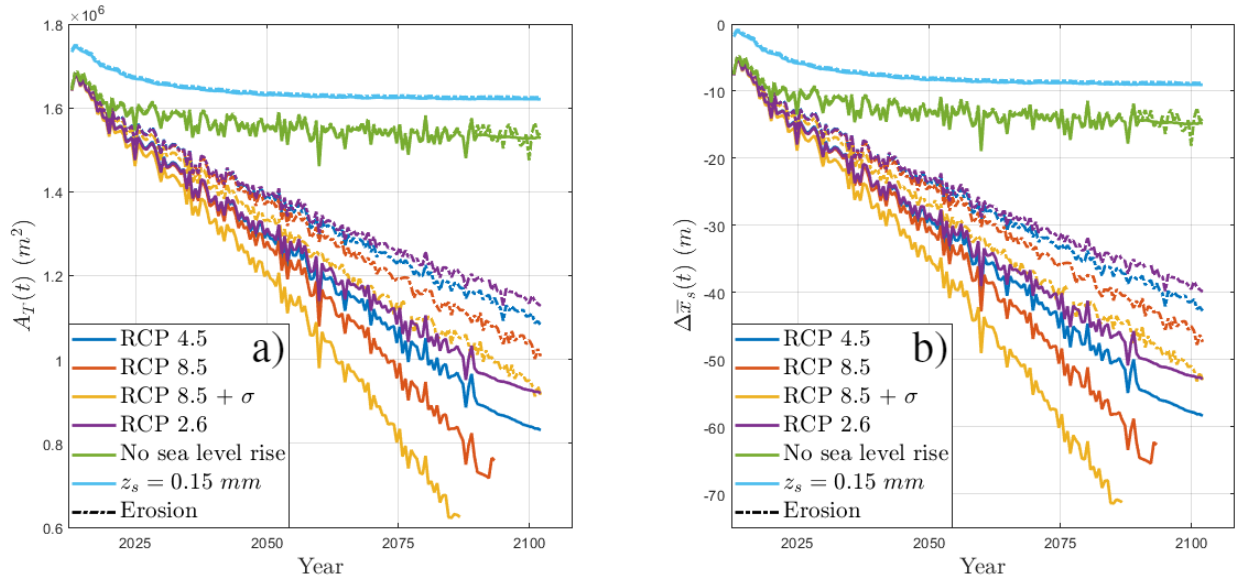

Figure 5.4.5: (a) Total dry beach area evolution over time for different MSLR scenarios in the last-minute simulations that skip NaNs. (b) Evolution of the modelled shoreline mean departure from the initial shoreline $(\Delta \overline{x}_s(t))$.
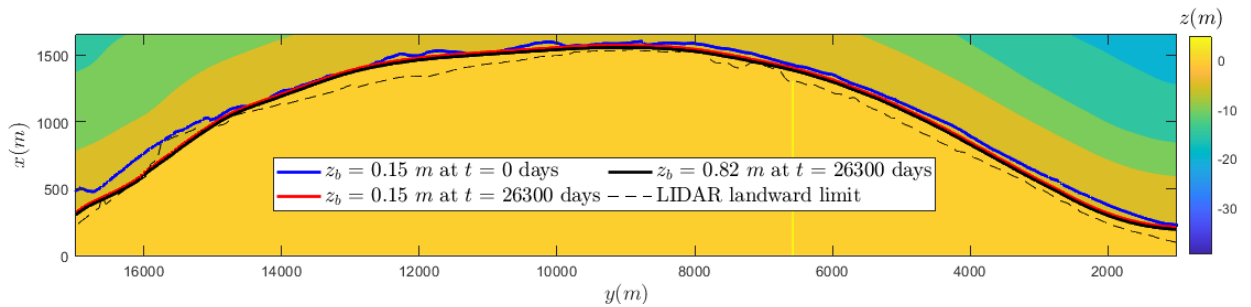

Figure 5.4.6: Shoreline obtained for Test 1 scenario RCP4.5 at $t = 32800$ days (year $\sim$2100) in the last-minute simulations that skip NaNs. Notice that the x-axis has been exaggerated to better discern the represented coastlines.

6   Conclusions and further work

6.1   Final remarks

Although the main goal of obtaining predictions for the evolution of the Llobregat delta in 100 years has not been fully accomplished, some guidelines on the characteristic morphodynamic behaviour of its regions have been established. From the tests conducted seems reasonable to assume that the area that will be most affected by the long-term effects of sea level rise will be the one closest to the Llobregat river mouth. Some of the Q2Dmorfo simulations predict that for the most likely climate change scenario, RCP8.5, this zone will experience a mean shoreline recession of over 120 m by 2080. For most locations within this region this recoil is more than the current dry beach width marked by LIDAR flights. These results are specially concerning when considering the proximity of large cities like El Prat de Llobregat or infrastructures like the Tarradellas international airport, which location lies in part within the limits of the expected shoreline regression. The predictions for the central and southernmost parts of the considered coast may not be that dramatic, but are also alarming. In overall, the RCP8.5 simulation estimates a total loss of 43% of the initial dry beach area and a mean coast recession of 50 m for year 2075. Even for scenarios RCP4.5 and RCP.2.6, which represent less severe predictions of sea level rise due to climate change, an area loss of over 35% has been obtained.

6.2   Future research and possible improvements

Clearly the first step towards improving this project is to determine whether if the numerical instability has a natural origin, or if it is just a modelling error or misinterpretation that needs to be fixed. For both situations, changes must be introduced to either adapt the Q2Dmorfo to properly handle the instability, or to completely avoid and suppress its signs without sacrificing precision. More observational research on the area next to the Llobregat mouth, $17000 > y > 15000$, would be also helpful to see if the modelled results match with the actual measurements.

Once this question is answered, there are still multiple ways to proceed. For example, having a better understanding and more data on the nearshore bathymetry would clarify if choosing the Castelldefels time-averaged beach profile as a proxy for all the cross-shore profiles in the reconstructed domain is a good approach, or if the initial bathymetry has to be reconsidered. The same reckoning applies to the equilibrium profile. Having more bathymetric measurements would allow to elucidate if the assumption in Q2Dmorfo model of an alongshore uniform equilibrium makes sense for this particular application. Performing more LIDAR flights would as well give a more accurate insight on the Llobregat delta coastline evolution and, in consequence, a more reliable validation process would be possible. Introducing some modifications on the model may also be in order. The first changes to consider are those related to the computation of the cross-shore transport. One proposal is to not depend on a unique equilibrium profile for all the domain, but on a z_{be} that changed with the alongshore position y. This would favour a better modelling of sites with curvilinear depth contours, as in the case of the Llobregat delta. Another approach would be to completely abandon the current strategy of relying on an equilibrium profile to model cross-shore sediment transport and introduce one based on physical computations, as it is done with the alongshore transport. Of course, that would imply a complete transformation of the Q2Dmorfo and probably would not be appropriate for obtaining long-term predictions, since the computational time needed would increase substantially. Also interesting would be to introduce the effect of diffraction in the Q2Dmorfo, allowing a better modelling of the areas immediately next to for the domain lateral groins.

e^f

7   Acknowledgements

e^f

Bibliography

[1] A. D. Sнokt, *Handbook of beach and shoreface morphodynamics*, John Wiley & Sons, 2000

[2] R. G. Dean , R. A. Dalrymple, *Coastal processes with engineering applications*, Cambridge University Press, 2004

[3] J. Fredsøe , R. Deigaard, *Mechanics of coastal sediment transport*, Advanced series on ocean engineering: Volume 3, 1994 (Second edition)

[4] P. D. Komar, *Beach processes and sedimentation*, Pearson Education, 1998 (Second edition)

[5] L. H. Holthuijsen, *Waves in oceanic and coastal waters*, Cambridge University Press, 2007

[6] J. Arriaga, *Dynamics of large-scale shoreline perturbations*

[7] R.L. de Swart, F. Ribas, D. Calvete et al., *Optimal estimations of directional wave conditions for nearshore field studies*, Continental Shelf Research, Vol. 196 (May 2020)

[8] P. Wang and N.C. Kraus, *Longshore Sediment Transport Rate Measured by Short-Term Impoundment*, Journal of Waterway, Port, Coastal, and Ocean Engineering, Vol. 125, Issue 3 (May 1999)

[9] R.E. Kopp, R.M. Horton, M. Oppenheimer et al., *Probabilistic 21st and 22nd century sea-level projections at a global network of tide-gauge sites*, Earth's future, Vol. 2, Issue 8 (August 2014)

[10] J.M. Sayol and M. Marcos, *Assessing Flood Risk Under Sea Level Rise and Extreme Sea Levels Scenarios: Application to the Ebro Delta* (*Spain*), Journal of Geophysical Research, Vol. 123, Issue 2 (February 2018)

[11] M. Meinshausen et al., *The RCP greenhouse gas concentrations and their extensions from 1765 to 2300*, Climatic change (Springer journal) 109, Article nº 213 (August 2011)

[12] J. Duro, J. Inglada et al., *High Resolution Differential Interferometry using Time Series of ERS and Envisat SAR Data*, Proceedings of the 2004 Envisat & ERS Symposium (September 2004)

[13] T.S. Bianchi, *Deltas and Humans: A Long Relationship Now Threatened by Global Change*, Oxford University Press (October 2016)

[14] L.O. Amoudry and A.J. Souza, *Deterministic Coastal Morphological and Sediment Transport Modeling: A Review and Discussion*, Reviews of Geophysics Vol. 49, Issue 2 (June 2011)

[15] Kamphuis and J. William, *Introduction to coastal engineering and management*, World scientific publishing (2000)

[16] Luijendijk, A. P. et al., *The initial morphological response of the Sand Engine: A process-based modelling study*, In: Coastal Engineering 119, pp. 1–14.

[17] Falqués, A., Ribas, F., Mujal-Colilles, A. & Puig-Polo, *A new morphodynamic instability associated to the cross-shore transport in the nearshore*, submitted to Geophys. Res. Letters (2020).

e**f**